UNIVERSITY OF OSLO
Department of Geosciences

Determination of the emission height profile of volcanic emissions using inverse modelling

Master thesis in Geosciences; Meteorology

Nina Iren Kristiansen

2 March, 2009

Abstract

An analytical inversion method is used to estimate the vertical profile of SO_2 emissions from the major eruption of Kasatochi volcano in Alaska in August 2008. The method uses satellite-observed total SO_2 columns and an atmospheric transport model to calculate the height emission profile. The Lagrangian particle dispersion model, FLEXPART, is used to simulate the transport of the emitted SO_2. The model simulations are based on meteorological analysis data provided by the European Centre for Medium-Range Weather Forecasts (ECMWF). Simulations are carried out for a large number of emission altitudes above the volcano where particles are released and subsequently tracked in the model atmosphere. The inversion method utilises the fact that winds normally change with height, and the misfit between the satellite observations and model results are minimised by combining emissions from different altitudes and also consider a priori information. Using satellite data for up to 72 hours after the eruption for the inversion, the estimated vertical profile yields emission maxima near 5 km above sea level (a.s.l), and around 9 and 12 km a.s.l, with smaller emissions above 15 km. The emissions reach an altitude of approximately 20 km, and the total mass of SO_2 injected to the atmosphere by the eruption was estimated to 1-1.2 megatons (Mt) with approximately 0.5 Mt reaching the stratosphere. Furthermore, a simulation of the transport extending for one month after the eruption is performed using the estimated vertical profile. This transport simulation is compared with independent satellite data and LIght Detection and Ranging (LIDAR) measurements of the volcanic plume to validate the retrieved emission height profile. The modelled plume agrees very well with SO_2 columns observed by AIRS, OMI and GOME-2, and the altitude agrees with ground-based LIDAR observations to within 1 km. The inversion result is robust against changes in the amount of observations used, however discrepancies were found regarding the use of weighting functions and observation uncertainties. The method is computationally very fast. It is therefore suitable for implementation within an operational environment, such as the Volcanic Ash Advisory Centers (VAACs), to predict the threat posed by volcanic emissions for air traffic. It could also be helpful for evaluating the sulphur input into the stratosphere, e.g., in connection to the proposed geo-engineering techniques to counteract global warming.

Acknowledgements

First of all I would like to thank my supervisor Andreas Stohl at NILU for excellent guidance and for answering my mails in the middle of the night. I also greatly appreciate the help from Sabine Eckhardt on running FLEXPART and understand the Matlab-world. Fred Prata has provided satellite data and was always very positive and encouraging. I also would like to thank NILU for supporting the trip to the IAVCEI conference on Island in August 2008. At the same time I thank the Department of Geosciences at University of Oslo for supporting the pre-conference field trip.

Thanks to my fellow students at CIENS, especially Karianne for going through this together with me. A special thanks to Silje and John for proof reading my thesis. Last but not least I would like to thank Rune for the homemade pizza and for keeping the apartment livable during this work.

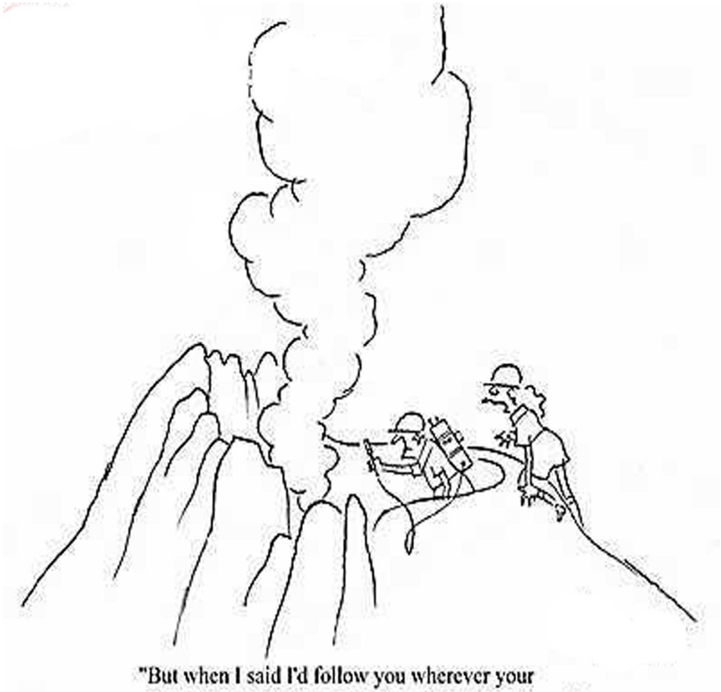

"But when I said I'd follow you wherever your career took you, I didn't know what a volcanologist was."

Abbreviations and acronyms

a.g.l	Above ground level
AIRS	Atmospheric InfraRed Sounder (on AQUA satellite)
AQUA	A NASA polar-orbiting satellite
a.s.l	Above sea level
ATHAM	Active tracer high resolution model
AURA	A NASA polar-orbiting satellite
AVO	Alaska Volcano Observatory
AWI	Alfred-Wegener-Institut für Polar- und Meersforschung
BrO	Bromine Monoxide
CALIOP	Cloud-Aerosol Lidar with Orthogonal Polarization (on CALIPSO satellite)
CALIPSO	Cloud-Aerosol Lidar and Infrared Pathfinder Satellite Observation
CloudSat	A NASA polar-orbiting satellite
DU	Dobson Unit (1 DU = 2.69×10^{16} molecules cm^{-2})
ECMWF	European Centre for Medium-Range Weather Forecasts
EUMETSAT	European Organisation for the Exploitation of Meteorological Satellites
FLEXPART	A lagrangian dispersion model
GEOS-CHEM	A global 3-D atmospheric composition model
GMS	Geostationary Meteorological Satellite
GOES	Geostationary Operational Environmental Satellite
GOME-2	Global Ozone Monitoring Experiment-2 (instrument on MetOp-A satellite)
HYSPLIT	HYbrid Single-Particle Lagrangian Integrated Trajectory
IPCC	Intergovernmental Panel on Climate Change
IR	InfraRed
LIDAR	LIght Detection and Ranging
LT	Local Time
MetOp-A	A polar-orbiting meteorological satellite operated by EUMETSAT
MLS	Microwave Limb Sounder (on AURA satellite)
MODIS	Moderate Resolution Imaging Spectroradiometer (on AQUA satellite)
MSG	Meteosat Second Generation (geostationary satellite operated by EUMETSAT)
Mt	Megaton (10^{12} gram)
MUT	Mid- and Upper-Troposphere
NAME	Numerical Atmospheric dispersion Modeling Environment
NASA	National Aeronautics and Space Administration

NILU	Norwegian Institute for Air Research
N_2	Nitrogen
OH	Hydroxyl Radical
OMI	Ozone Monitoring Instrument (on AURA satellite)
OsloCTM2	Oslo Chemical Transport Model version 2
PARASOL	A French-built polar-orbiting research satellite
RADAR	RAdio Detection And Ranging
SEVIRI	Spinning Enhanced Visible and Infrared Imager (on MSG satellite)
SO_2	Sulphur dioxide
TES	Tropospheric Emission Spectrometer (on AURA satellite)
Tg	Teragram (10^{12} gram)
UTC	Coordinated Universal Time
UTLS	Upper Troposphere and Lower Stratosphere
UV	UltraViolet
VAAC	Volcanic Ash Advisory Center
VEI	Volcanic Explosivity Index
WMO	World Meteorological Organization

Contents

Chapter 1

Introduction

Life on Earth is affected by the powerful forces of our Inner Earth - volcanoes! The gaseous emissions of the volcanoes are a natural part of our lives being the main source of our atmosphere and oceans which make it possible to live on our planet. For people living close to an active volcano, everyday life is certainly affected by the presence of the potential hazardous flaming mountain. Even if one has never even seen a volcano in real life, one is still affected by them through e.g. the climatic effects and potential long transported material from an eruption. Volcanoes are also responsible for the most beautiful red sunsets. Even walking into a museum can be a part of a volcanic experience. The famous 1893 Edvard Munch painting, "The Scream", shows a red volcanic sunset over the Oslo harbour. Scientists believe Munch was inspired by the 1883 Krakatau eruption in Indonesia which caused a red sky over Europe during the winter following the eruption (Olson et al., 2003).

Roughly 60 volcanoes erupted each year during the 1990s and probably at least 20 volcanoes will be erupting as you read these words. Italy's Stromboli, for example, has probably been erupting for more than two thousand years (Smithsonian Institution, 2008). Volcanic eruptions inject several different types of particles and gases into the atmosphere. Generally, the major component is tephra, also called ash, which is solidified material. The most abundant gases emitted are water vapour (H_2O), carbon dioxide (CO_2) and nitrogen (N_2). It is these gases that have been the main source of the Earths atmosphere and ocean (Robock, 2000). Another important gas emitted by volcanic eruptions is sulphur dioxide (SO_2) which will be the gas explored in this thesis.

The effects of volcanic eruptions are several and complex, but in principle volcanic eruptions perturb the radiation balance of the Earth and are also a threat to airline traffic. Volcanic eruptions can cause changes in the global climate by emissions of SO_2, which is converted to sulphate particles in the atmosphere. If the sulphate stays in the troposphere, it will have insignificant effect on the climate because of its short residence time there. But if large amounts of SO_2 are emitted deep into the stratosphere where the sulphate particles have long residence time, they will affect the Earth's radiation balance by scattering sunlight and thus increase the Earth's albedo and cool the planet (Textor et al., 2003).

Volcanic ash is a great danger to aircraft flying near ash clouds because the ash can cause dangerous damage, and even loss of power on one or more engines. In June 1982, for example, a British Airways Boeing 747 lost all four engines and suffered severe damage when flying into a volcanic ash cloud over Indonesia. The aircraft descended to 12,000 feet before being able to restart some engines and make an emergency landing in Jakarta. Today there are nine Volcanic Ash Advisory Centers (VAACs) around the world which are responsible for advising international aviation of the location and movement of clouds of volcanic ash. The VAACs use satellite information, ground reports from volcanological agencies, pilot reports, meteorological knowledge and numerical models to track and forecast ash movement so that aircraft can fly around the airborne ash safely (VAAC, 2008)

One major goal of this study of volcanic effects is to accurately predict the transport of volcanic emissions. One way of approaching this goal is by numerical modelling of the volcanic plume. In order to perform a numerical simulation of the volcanic plume, information on the time of eruption onset and duration, wind fields, loss of the emitted species etc. is required. Another important parameter for the numerical simulation is the vertical emission height profile of the volcanic eruption, that is, how much mass is emitted at distinct height levels above the volcano. The warnings of VAACs are based on numerical simulations of the volcanic emission. The London VAAC, for example, need to have information on the location, start time, release height and top and bottom of the plume to initiate a run of the NAME model (Numerical Atmospheric dispersion Modelling Environment) (VAAC, 2008). Without accurate information on the release height, a crude assumption has to be made about the vertical profile for the volcanic emissions.

Unfortunately the emission height profile of a volcanic eruption is difficult to determine. Several earlier studies have investigated this issue. In general, the altitude of volcanic ash and sulphur injections into the atmosphere is poorly constrained by direct observations. The following is an overview of previous and other ongoing projects regarding height emission profiles of volcanic eruption.

- Local observers can often give a hint on the emission height of ash, but this is always of unknown accuracy, and most often the volcanic eruption is not observed by eye witnesses at all. Also of consideration is the SO_2 which is invisible to the naked eye.

- Aircraft measurements can also be made to determine the plume height (Mankin et al., 1992), but such observations are not normally available. Even research aircraft will normally not fly into the plume for safety reasons.

- Weather Radio Detection And Ranging (RADAR) or Light Detection and Ranging (LIDAR) observations at ground can determine the plume height (Wang et al., 2008). The disadvantage is that not all locations are covered by such observations.

- Numerical modelling can give information of the plumes vertical distribution. The Active tracer high resolution model (ATHAM) is a prognostic eruption-column model which uses the mass flux of pyroclastic material[1] and ambient atmospheric conditions to estimate the vertical emission (Oberhuber et al., 1998; Textor et al., 2003). The problematic issue about this model is getting appropriate input data.

- Remote sensing observations from satellites can provide global coverage but they normally only deliver total columns (e.g., SO_2) or very poorly resolved vertical profiles.

- Space based LIDAR, such as the Cloud-Aerosol Lidar with Orthogonal Polarization (CALIOP) on board the Cloud-Aerosol Lidar and Infrared Pathfinder Satellite Observation (CALIPSO) platform, can provide excellent height estimates for aerosols, but both the horizontal spatial sampling and temporal coverage is poor (NASA, 2008). Therefore there are no reliable height estimates available from satellites for operational use.

- One analysing technique involves trial-and-error fits between observations of the clouds and model results by guessing the height of the cloud. The HYbrid Single-Particle Lagrangian Integrated Trajectory (HYSPLIT) model, for example, can be used with satellite measurements of SO_2 from the Ozone Monitoring Instrument (OMI), to fit trajectories at certain altitudes with the observations (Carn et al., 2008a). The disadvantage with this method is that the model runs and satellite data are matched "by eye". This is a subjective process that is time-consuming and can lead to errors.

---

[1] Pyroclastic material is another name for a cloud of vapour and rock fragments of explosive origin (e.g., ash and lava fragments). Pyroclastic flows are usually very hot, move rapidly due to buoyancy provided by the vapours, can extend miles from the volcano, and devastate life and property within their paths.

- Another technique is based on backward trajectory analysis using ensembles and dispersion modelling which can also provide information on emission heights (Maerker et al., 2008). The model calculations are initialised by satellite observations of a volcanic plume, this means that the model performs emissions of SO_2 at different height levels, at the location of the satellite observations. Backward trajectories are calculated, and the trajectories that pass over the volcano at distinct height levels at the time of eruption are counted. This results in a distribution of the most probable emission heights. The disadvantage with this technique is that it only provides simple and qualitative estimates for the height emission profile.

- New methods in satellite data can potentially provide information on the SO_2 vertical distribution by calculating an OMI-AIRS residual SO_2 column. Atmospheric InfraRed Sounder (AIRS) is a satellite instrument measuring in the infrared region. The AIRS SO_2 retrievals are typically restricted to the upper troposphere and lower stratosphere (UTLS) (Prata and Bernardo, 2007), while OMI provides total column SO_2 measurements. A lower tropospheric SO_2 cloud would produce a large residual making it possible to estimate the SO_2 vertical distribution in the lower troposphere (Carn et al., 2008a).

In this thesis the goal is to study the emission height profiles of a volcanic eruption through an inversion method that uses both simulated and observed columns of SO_2. This method uses the column quantities from satellite observations together with a transport model to determine the vertical emission profile. A large number of simulations of emission transport from different altitudes above a volcano are performed using a Lagrangian particle dispersion model, FLEXPART. Remote sensing data of SO_2 total columns from different satellite instruments are used to obtain a linear combination of the model runs. The vertical profile obtained should, as well as possible, reconstruct the observed spatial pattern. This takes advantage of the fact that emissions at different altitudes are transported into different directions because of vertical wind shear, and thus the spatial patterns of SO_2 columns bring information on the plume's altitude. For determining the optimum linear combination, a formal analytical inverse modelling framework is used. The inversion method is tested for one specific volcanic eruption, and the accuracy of the method is determined.

Chapter 2

Background

In this section a short introduction to volcanoes and their main effects is given, starting with volcanoes and volcanic eruptions in general, moving on to the transport of volcanic eruption plume, their effects on climate and aviation, and finally the volcanic eruption of Kasatochi investigated in this thesis is elaborated.

2.1 Volcanic eruptions

Volcanoes are generally found where tectonic plates are diverging or converging. The Mid-Atlantic Ridge has examples of volcanoes caused by "divergent tectonic plates" pulling apart. Most divergent plate boundaries are at the bottom of the oceans, therefore most volcanic activity is submarine, forming new seafloor. The Pacific "Ring of Fire", encircling the basin of the Pacific Ocean, has examples of volcanoes caused by "convergent tectonic plates" coming together. By contrast, volcanoes are usually not created where two tectonic plates slide past one another. Volcanoes can also form where there is stretching and thinning of the Earth's crust such as in the African Rift Valley and the Rio Grande Rift in North America. Moreover, volcanoes can be caused by "mantle plumes" often far from plate boundaries. The volcanoes at Hawaii are examples of volcanoes caused by these so-called "hotspots".

During a volcanic eruption large amounts of solid matter and gases are emitted to the atmosphere. The major component is ash. Water vapour (H_2O) is typically the most abundant volcanic gas, followed by carbon dioxide (CO_2), nitrogen (N_2), and sulphur dioxide (SO_2). The mass loadings of a volcanic eruption varies from one eruption to another. The extreme eruption of Mount Pinatubo in the Philippines in June 1991, emitted an estimated 20 megatons (Mt) of SO_2 to the atmosphere (Bluth et al., 1993).

The duration of a volcanic eruption varies substantially. A few volcanoes have been erupting more or less continuously through the last three decades, other eruptions end swiftly. Most end in less than 3 months, and few last longer than 3 years. The median duration is about 7 weeks (Smithsonian Institution, 2008).

There are many different kinds of volcanic activity and eruptions. The main classification involves explosive and non explosive eruptions. Several measuring units exists for defining volcanic eruption, for example, Volcanic Explosivity Index (VEI) which records how much volcanic material is thrown out, how high the eruption goes, and how long it lasts. The index ranges from 0, being non-explosive, to 8, a mega-colossal eruption. The eruption of Mount Pinatubo in 1991 was a category 6 eruption termed colossal. For non explosive eruptions, the injection height can be on the order of a few hundred meters and is dominated by thermal plume rise. Explosive eruptions have a considerable initial exit velocity, followed by buoyant convection due to entrainment and heating of air by the hot ash. The thermal energy in explosive eruption plumes allows them to quickly reach high altitudes. Generally the injection height depends on the kind of eruption and meteorological parameters (Oberhuber et al., 1998), such as the wind, humidity and stratification. For moderate-scale explosive eruptions, 20% of volcanic plumes rise higher than 15 km, 60% rise above 10 km, and 80% rise above 6 km (Halmer and Schmincke, 2003). For the eruption of Mount Pinatubo in June 1991, gas and particles were carried to an altitude of more than 30 km (McCormick et al., 1995). Once the species are injected into the stratosphere they are rapidly advected around the globe.

2.2 Transport

The dispersion of volcanic clouds depend heavily on the meteorological settings at the time of the eruption. As an example, the two volcanoes El Chichón (17° N) and Pinatubo (15° N) are separated by only 2°, however the eruptions in 1982 and 1991, respectively, resulted in clouds separated by as much as 15° after only one circuit of the globe (Robock, 2000).

Even though the local atmospheric winds play a significant role for the dispersion, it is possible to say something about the likelihood of a volcanic cloud in a distinct height, spreading in a certain direction based on the mean wind circulation patterns.

The general circulation of the troposphere is often described by a three-cell model, as illustrated in figure 2.1. The three circulation cells; the Hadley cell, the Ferrel cell and the Polar cell, form the Trade winds and the Westerlies which are dominating the horizontal transport in the troposphere. Volcanic clouds in the lower troposphere would tend to follow these main transport patterns, e.g., volcanic clouds from equator to ∼30° N will mainly be transported westward. In the contrary case, volcanic emissions are transported mainly eastward when they occur between ∼30°-60° N.

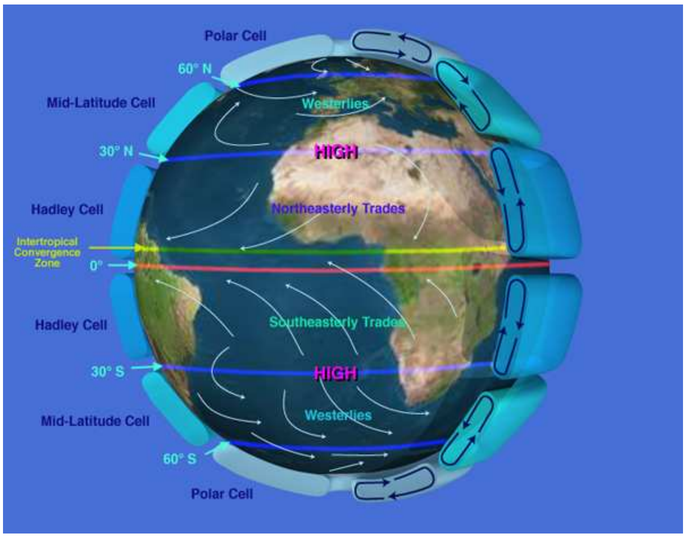

Figure 2.1: *Illustration of the global circulation cells and wind patterns. (Source: http://sealevel.jpl.nasa.gov/overview/climate-climatic.html).*

In the mid- and upper-troposphere (MUT), zonal winds are stronger than meridional winds. The strong zonal jets at around 10 km altitude are found at roughly 30° N in January and 30° S in July, the latter one can be identified in figure 2.2(a) which shows the long-term mean zonal wind fields at 250 hPa (∼10 km) for August. Consequently, in the MUT, volcanic clouds tend to travel rapidly in the zonal direction. Zonal winds are generally quite weak at 10° S and 10° N of the equator, but there is noticeable seasonal dependence, with easterlies dominating the latitudes north of equator in August, as seen on the figure. The eruptions that occur north and south of 10° will spread volcanic debris in directions and at speeds that depend on the hemisphere and the season. Figure 2.2(b) shows the latitude-height cross section of the long-term mean zonal winds for the northern hemisphere in August, with the strongest zonal wind found at 250hPa around 40°-50° N . The wind patterns change significantly with height, it is therefore critical to know the emission height of the eruption to determine where it will disperse.

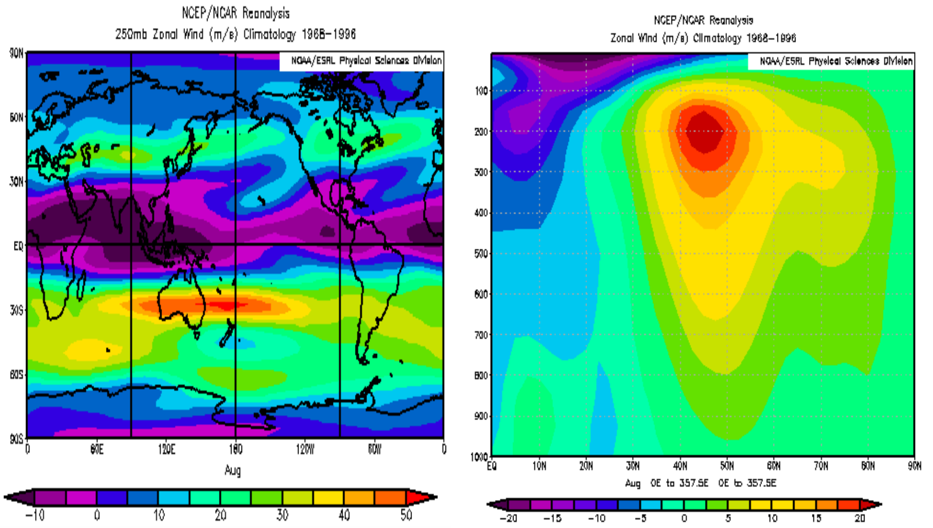

(a) (b)

Figure 2.2: *Long-term mean zonal wind in m/s for August. a) Horizontal fields at 250hPa b) Latitude by height cross section. From NOAA/ESRL Physical Sciences Division, see: http://www.cdc.noaa.gov/cgi-bin/data/composites/printpage.pl*

2.3 Effects on climate

Of the most abundant gases emitted during a volcanic eruption, both H_2O and CO_2 are important greenhouse gases, but their atmospheric concentrations are so large that individual eruptions have a negligible effect on their concentrations and do not directly impact the greenhouse effect (Robock, 2000).

The most important climatic effect of explosive volcanic eruptions is through emission of sulphur species deep into the stratosphere, mainly in the form of sulphur dioxide (SO_2). It is a colourless gas with a characteristic odour. The background atmosphere contains very little SO_2. Most anthropogenic sources come from industry whilst natural emissions are dominated by volcanic sources (Brasseur et al., 1999).

In general the effects of SO_2 emissions by volcanic eruptions depend on the height of the emitted gas, hence if it stays in the troposphere or is injected into the stratosphere. When SO_2 is emitted to the troposphere it is potentially harmful to human health by causing eye irritation, breathing difficulties and death when encountered in high concentrations. When a volcanic plume containing SO_2 mixes with atmospheric moisture, acid rain forms. Acid rain can significantly reduce the growth of plant life (Brasseur et al. (1999)). In the troposphere gas phase oxidation of SO_2 by hydroxyl radical OH forms sulphate. The lifetime[1] of SO_2 and sulphate in the troposphere is on the order of a few days (e.g., Berglen et al. (2004)), limiting the climatic impact.

SO_2 in the stratosphere has a significant impact on global climate. Volcanic eruptions produce most of the SO_2 in the stratosphere, and SO_2 and other sulphur-based gases are believed to be the primary precursors of stratospheric aerosols (Liou, 2002). The SO_2 converts to sulphate aerosols which is of specific importance to climate due to their long residence time in the stratosphere. The transformation of SO_2 to aerosols in the stratosphere is by chemical reaction with OH and H_2O on a timescale of weeks (Bluth et al., 1997). The resulting sulphuric acid (H_2SO_4) rapidly condenses into aerosols because it has a very low saturation vapour pressure. The sulphate aerosols produced are about the same size as visible light, with a typical effective radius of 0.5 micrometres and have a single scattering albedo of 1 (Robock, 2000). They therefore strongly interact with solar radiation by scattering. The aerosols reflect some solar radiation back to space, thus increasing the Earths albedo (Textor et al., 2003) by a direct radiative effect. As a result the Earth's surface will be cooled by the reduced amount of solar radiation reaching the surface. In contrast, the aerosols in the stratosphere will absorb both upwelling infrared radiation from the troposphere and surface, as well as some solar radiation, and the result is heating of the stratosphere, as illustrated in figure 2.3.

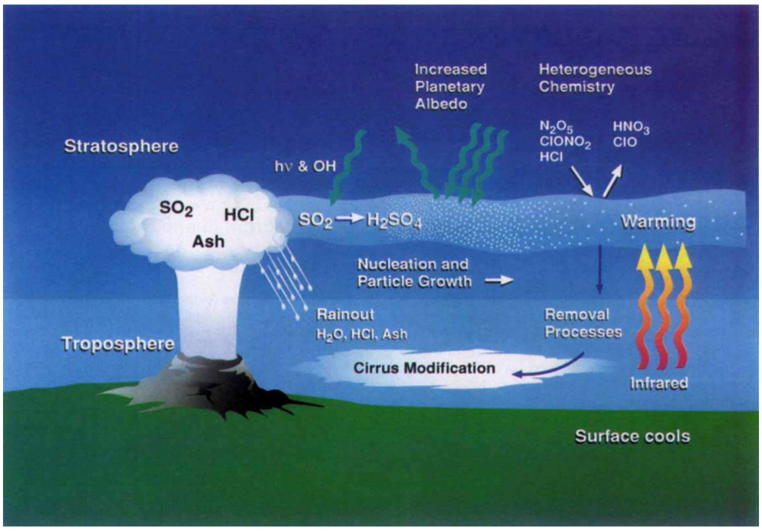

Figure 2.3: *Volcanic effects on climate. Source: McCormick et al. (1995)*

---

[1] The atmospheric lifetime of a species is defined as the average time it takes for the abundance of a molecule to be reduced by a factor 1/e, also known as e-folding time.

The radiative forcing produced by the enhanced anthropogenic sulphate aerosol burden since preindustrial times is estimated to be approximately -0.5 W/m^2, see figure 2.4. The value was updated to -0.4 ± 0.2 W/m^2 in the IPCC Fourth Assessment Report. This negative forcing partially offsets the larger (about 2.4 W/m^2) warming effect of greenhouse gases.

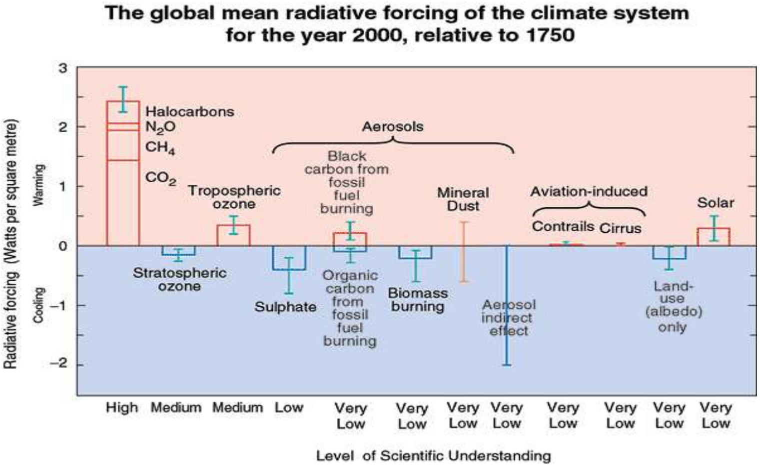

Figure 2.4: *External factors force climate change. Forcing due to episodic volcanic events, which lead to a negative forcing lasting only for a few years, is not shown. From: IPCC (2001).*

Because of the episodic and transitory nature of volcanoes, it is difficult to give a best estimate for the volcanic radiative forcing. Global climate modelling suggest that the radiative effect of volcanic sulphate is only slightly smaller than that of anthropogenic sulphate, even though the anthropogenic SO_2 emissions are about five times larger (IPCC, 2001). The main reason is that SO_2 is released from volcanoes at higher altitudes where the residence time of SO_2 is longer mainly due to low dry deposition rates. The explosive 1991 Mount Pinatubo is the only major eruption that is well-documented. It is estimated that a radiative forcing of about -4 W/m^2 was reached approximately six months after this eruption (McCormick et al., 1995). There have been no explosive and climatically significant volcanic events since Pinatubo and the global stratospheric aerosol concentrations are currently very low (Forster et al., 2007b).

Recently it has been suggested that injecting sulphur into the stratosphere could be used as a strategy to reduce global warming due to increasing CO_2 levels (e.g., Crutzen (2006); Wigley (2006)). It is believed that emissions of a large amount of sulphate into the stratosphere will cause surface cooling that to some extent can offset the global warming by greenhouse gases. Such a drastic tampering with the Earth's climate requires very careful consideration. At the present, the annual injection of SO_2 into the stratosphere from volcanoes is poorly known. However, volcanic eruptions are a natural source of sulphate in the atmosphere and can be used to study the consequences of emitting large amounts of sulphate into the atmosphere.

The equatorial region is specially important for stratospheric gas injection because it is the area with the highest frequency of eruptions. Furthermore, gas injected into the stratosphere in equatorial areas can quickly be transported around the globe by winds and also into both hemispheres (Halmer and Schmincke, 2003). However, eruptions in the tropics have to be more powerful to inject gas into the stratosphere than eruptions at high latitudes because the tropopause rises from approximately 9-11 km at the poles to 15-16 km in the equatorial region (0°-30°North). For the polar region, stratospheric winds tend to push sulphate aerosols towards the poles and towards the surface, hence limiting the area influenced by the aerosols.

Another reason for the importance of tropical volcanic eruptions is an atmospheric dynamical response to large tropical volcanic eruptions. Tropical volcanic eruptions can cause tropospheric warming rather than an enhanced cooling over Northern Hemisphere continents. The lower stratospheric heating by aerosols is much larger in the tropics than at the poles as there is more sunlight present near equator. The tropical heating increases the Equator-Pole temperature gradient and makes the jet stream (polar vortex) stronger. The strengthened polar vortex traps the wave energy of the tropospheric circulation, and the stationary wave pattern known as the North Atlantic Oscillation (NAO) circulation pattern is amplified. This advective effect dominates over the radiative effects in the winter, producing winter warming over Northern Hemisphere continents (Robock, 2000).

Other climatic effects by sulphate include indirect radiative effects where the sulphate particles can act as cloud condensation nuclei in the troposphere (Textor et al., 2003). By increasing the number of droplets and decreasing their size, the optical properties of the clouds are changed, e.g., the reflectivity of the cloud is enhanced. This can possibly be involved in a climate feedback loop. In addition, the precipitation efficiency is reduced and the cloud water content and lifetime of clouds are increased. Both the direct radiative effect and these indirect radiative effects contribute to a cooling of the Earth's surface (IPCC, 2001). Furthermore, the sulphate aerosols in the stratosphere can provide sites for heterogeneous reactions that can cause ozone depletion on a global scale. Analyses of long-term global observations have shown a reduction in global mean ozone amount of about 4 % following the Mt. Pinatubo eruption (Brasseur et al., 1999). Volcanic effects may persist for 2-3 years after a major eruption, roughly the stratospheric residence time of the sulphate aerosols.

2.4 Aviation hazard

Volcanic ash can cause extensive damage to aircraft flying into ash clouds. The ash can cause machinery damage and even complete engine shut-down. Also the windscreens of the aircraft are scraped off by the ash reducing sight. This is extremely dangerous for safety reasons, in addition, the ash encounters can cause very expensive damage to the aircraft.

The problems with volcanic clouds affecting air traffic are many. Volcanic eruptions are highly unpredictable both in time and location, however on average eruptions occur about once per week somewhere on the globe. Most volcanoes are remote and observed rarely. The volcanic emissions can spread a long distance in just a few hours, moreover the fine ash particles do not show up on the aircraft's radar and cannot be seen at night or in clouds. It can also be difficult to discriminate hazardous volcanic clouds from more common meteorological clouds by the naked eye.

Many commercial aircraft cruise at an altitude between 10-13 km to exploit the high velocity jet stream winds ($\sim$100m/s) to save time and fuel. Volcanic eruptions that inject material to altitudes of $\sim$10 km may pose a great threat to these airroutes. The high wind speeds at this altitude will potentially transport the emitted material over long distances in just a few hours, so that volcanic debris can be found far from its source. Occupying the jet stream currents, aircraft may risk extended contact with volcanic gases and particles.

Identifying hazardous volcanic ash in the atmosphere, and especially determining the vertical distribution of the cloud during transport is performed with large difficulties. When an eruption occurs, the ash and gas are probably spread throughout the vertical column of the atmosphere from ground up to the maximum height reached by the volcanic cloud. During the first few hours after the eruption, the areas in the vicinity of the volcano poses the greatest threat to aviation. Following an eruption, the ash and gases can be transported over great distances. During this transport the ash and gas are usually restricted to a much smaller vertical range of 1-2 km. However, currently there is not sufficient information available on where the cloud is localised in the vertical. Furthermore, the level of minimum ash concentration level dangerous to aviation is not known accurately. For these reasons, the current practice is to warn aircraft pilots to fly around a rather large spatial region which is determined by the horizontal location of the cloud, as well as the vertical region from ground up to the flight level affected. But because the volcanic cloud usually is confined to a layer of 1-2 km, this strategy is perhaps unnecessary and is clearly a financial burden for the airline companies. By knowing the injection height profile of an eruption, it will be possible to forecast the cloud movement with greater accuracy and provide reliable information on where the cloud is localised in the vertical. By offering height and horizontal spatial information of the location and movement of volcanic clouds, and also by specifying a critical ash concentration level, the aviation industry will be able to re-route air traffic as necessary for safety reasons, and at the same time minimise the extra cost by decreasing the use of fuel.

Today there are nine Volcanic Ash Advisory Centers (VAACs) around the world, appointed by the World Meteorological Organization (WMO). They work as a link between meteorologists, volcanologists and the airline industry. They issue warnings about the location and movement of clouds of volcanic ash. The VAACs include the use of numerical models to track and forecast ash movements, and continuous improvements on the modelling of the dispersion is an important part of their work.

There are several concerns about modern developments in the aviation industry regarding the effects of hazardous volcanic clouds on aviation. Air traffic is growing globally and in the future the Asian Pacific region is likely to be the most vulnerable for volcanic cloud encounters because of the large number of volcanoes present, and the increasing rate of air traffic (Prata, 2008). In addition, modern developments in aircraft show an increasing trend towards 2-engine jets, away from 4-engine aircraft. With fewer engines the risk of complete loss of power is amplified.

Volcanic gases, specifically SO_2 may also pose a hazard to aircraft, however the extent of this threat is not known exactly. It is possible that SO_2, in sufficiently high concentrations could cause fuel contamination, and if encountered as sulphuric acid aerosol, it is believed that window damage could also occur (Bernard and Rose, 1984). It is generally assumed that the emission of SO_2 will be accompanied by ash. Therefore, pilots are trained to recognise the acrid odour generated by sulphur gases. If the gas is detected they should take precautions and report it. Under the assumption that volcanic SO_2 in the upper troposphere travels with volcanic ash, it is sensible to use satellite measurements of SO_2 as a proxy for volcanic ash. Also since SO_2 is easier to measure using remote techniques, it is often preferred to use SO_2 measurements. However, in some cases gas and ash can be separated and travel in different directions and at different heights in the atmosphere. This can be due to the different specific gravities of gas and ash (Holasek et al., 1996). It might also be possible that the emissions of gas and ash happen during different phases of the eruption and in that way are separated. The theory of separation has been documented by cases investigated by Prata and Kerkmann (2007) and Schneider et al. (1999) and needs further research.

2.5 Kasatochi Volcano, Alaska

Kasatochi Volcano (52.17°N, 175.51°W) is a small unpopulated 2.7×3.3 km wide island volcano in Alaska, situated on the Aleutian arc. The active stratovolcano reaches only 314 m above sea level, and the 750-m-wide crater contains a saltwater lake (Smithsonian Institution, 2008).

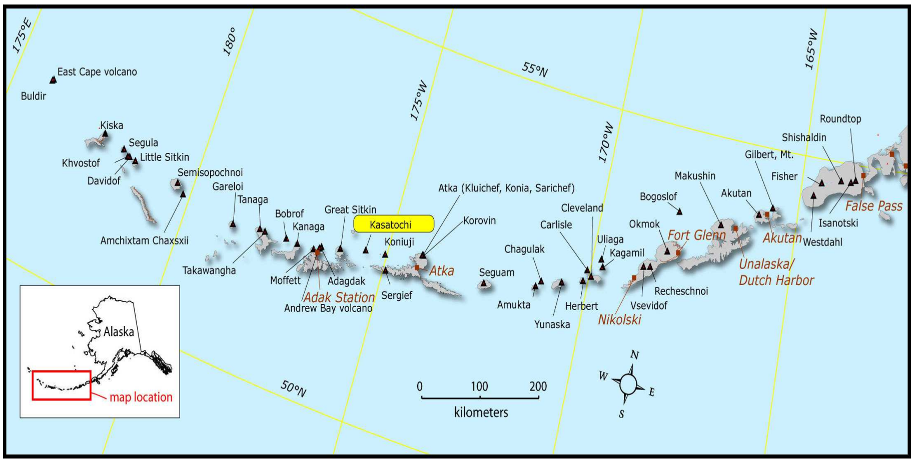

Figure 2.5: *Position of Kasatochi Volcano. Source: AVO*

From 7-8 August 2008 the volcano erupted with little warning. It had not erupted in at least 200 years. The eruption emitted one of the largest volcanic sulphur dioxide clouds scientists have observed since Chile's Hudson volcano erupted in August 1991 and emitted approximately 1.5 teragrams (Tg) of SO_2 into the atmosphere. For Kasatochi the maximum mass loadings of SO_2 were found to be about 1.2-1.5 Tg (e.g., NASA (2008); Rix et al. (2008)). The eruption also injected an amount of ash into the atmosphere. Alaska Airlines was forced to cancel 44 flights between the 10 and 11 August 2008 (O'Malley and Bragg, 2008). The ash particles got deposited after a few days, while the SO_2 dispersed throughout the whole northern hemisphere. Furthermore, Theys et al. (2009) detected large enhancements of bromine monoxide (BrO) by the Global Ozone Monitoring Experiment-2 (GOME-2) satellite instrument in the vicinity of Kasatochi in the days following the eruption.

The exact time of the eruption is not known since the crater was covered by clouds and thus eye witnesses were not able to make any observations. On the morning of 7 August, Alaska Volcano Observatory (AVO) reported increased earthquake activity and volcanic tremors, as well as observations of a strong sulphur smell by a US Fish and Wildlife Service field crew on the island. The same day satellite data showed an ash plume to an altitude of at least 10 km in the vicinity of Kasatochi Volcano at 22:30 UTC. On 8 August, AVO reported that three major explosive eruptions occurred at Kasatochi between approximately 22:00 UTC on 7 August and 04:35 UTC on 8 August. Ash from these explosions reached at least 13.5 km above sea level and produced a continuous ash cloud.

The meteorological conditions at the Aleutian arc shortly before and after the eruption are illustrated in figure 2.6 with geopotential heights, given in decametre (dkm), on the pressure levels 1000hPa and 500hPa. The geopotential heights are taken from the European Centre for Medium-Range Weather Forecasts (ECMWF) analysis. The figures show a small cyclone south of the volcano in the hours before the eruption. During the eruption the low pressure system moves eastward, and roughly 12 hours after the eruption the cyclone is found southeast of the volcano. Consequently, due to the flow in the cyclone, the volcanic plume became "croissant"-shaped within one day after the eruption. Later the plume was transported into a distinct circular shape.

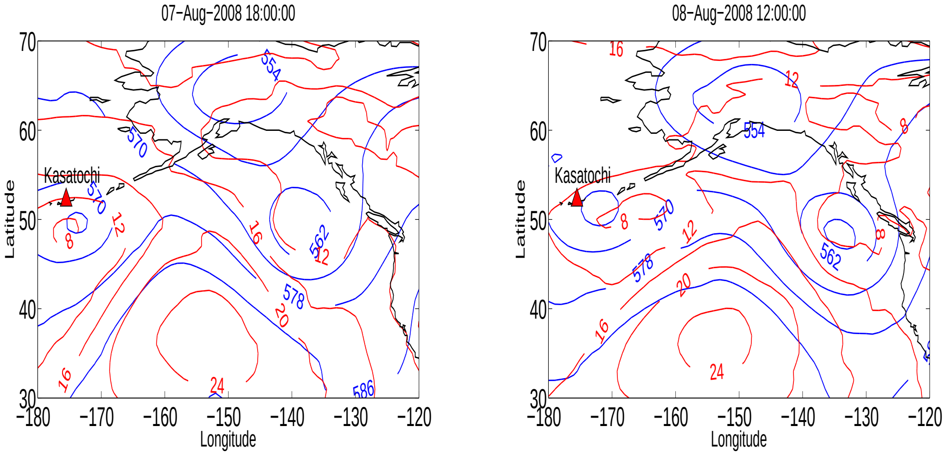

(a) (b)

Figure 2.6: *Geopotential height [dkm] on pressure levels 1000hPa (red line) and 500 hPa (blue line), for the hours shortly before and after the eruption of Kasatochi. From the ECMWF analysis.*

After drifting over the Pacific Ocean, the SO_2 cloud was transported over North-America, reaching Europe in one week then taking another seven days to reach Alaska again.

Several satellite instruments (e.g., AIRS, OMI, GOME-2, MODIS) were able to observe the volcanic cloud emitted by the eruption of Kasatochi. On 8 August, the day after the eruption, skies were cloudy when the Moderate Resolution Imaging Spectroradiometer (MODIS) on NASA's Terra satellite passed overhead and captured the natural-colour image shown in figure 2.7(a). The bright clouds provided good contrast for the volcanic plume, which is dark brown. The distinct "croissant"-shape of the plume is clearly visible. Figure 2.7(b) shows the SO_2 plume detected by the GOME-2 instrument on the MetOp-A polar-orbiting satellite, on 12 August, 5 days after the eruption, when the plume has moved over North-America.

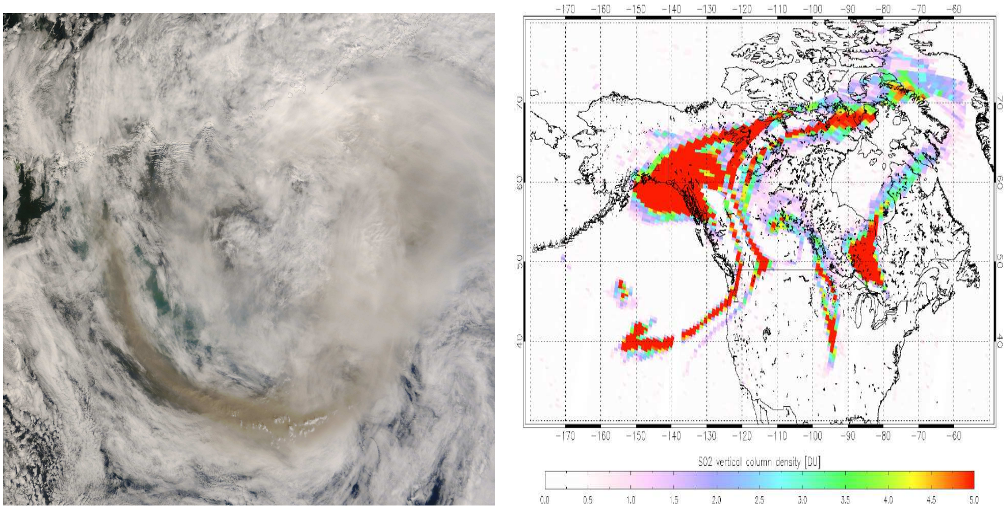

(a) MODIS, 8 August

(b) GOME-2, 12 August

Figure 2.7: *a) Volcanic ash plume from the Kasatochi eruption, as detected by MODIS on 8 August 2008. From: NASA (2008) image by Jeff Schmaltz. b) The Kasatochi volcanic SO_2 plume detected on 12 August by the GOME-2 instrument. From: Rix et al. (2008)*

Chapter 3

Methodology

The inverse method used in this study makes use of an atmospheric transport model and satellite data. Generally, a simulation of the volcanic eruption, for a few days following the eruption, is done with a numerical model. Appropriate input data for the eruption, e.g. time of eruption onset and location is needed and an a priori height emission profile is assumed. Together with corresponding satellite data for the eruption, the inverse method is applied to give an estimated height emission profile of the volcanic eruption. This section describes first the numerical model used, secondly a description of the different satellite data used, and finally the inverse method is described in more detail.

3.1 FLEXPART

The numerical model used in this thesis is the atmospheric trajectory and particle dispersion model, FLEXPART (Stohl et al. (2005, 1998), see also `http://transport.nilu.no/flexpart`). The model was originally developed to simulate the dispersion of dangerous substances from point sources, such as after an accident in a nuclear power plant. At the present, the main applications for the model are atmospheric transport of radionuclides after nuclear accidents, pollution transport, greenhouse gas cycles, stratosphere-troposphere exchange, water cycle research and others. The model was developed by Andreas Stohl and mainly people from NILU, Institute of Meteorology in Austria and the Preparatory Commission for the Comprehensive Nuclear Test Ban Treaty Organization in Vienna, Austria. It is now used by a large number of research groups in many different countries.

FLEXPART is a Lagrangian particle dispersion model which calculates so-called trajectories by following "tracer particles" as they are displaced by the winds. Lagrangian methods are generally used to determine, for example, the transport over several days of an air parcel released at a given location in the atmosphere. Lagrangian algorithms are frequently used in regional pollution studies, that is, to compute the dispersion of pollutants in industrialised areas. Lagrangian models are simple in concept and, unlike Eulerian models, are not subject to numerical diffusion which can damp out or smooth differences in the tracer field. Furthermore, Lagrangian models are independent of computational grid and can in principle have infinitesimally small resolution.

By releasing a large number of tracer particles (not necessarily representing real particles, but infinitesimally small air particles) FLEXPART can simulate the long-range and mesoscale transport, diffusion, convection, dry and wet deposition, and radioactive decay of these released tracers. The model can be used forward in time to simulate the dispersion of tracers from their sources, or backward in time to determine potential source contributions for tracers reaching a given location in the atmosphere. The model is an off-line model which can use meteorological fields (analysis or forecasts) from a variety of global and regional models, most commonly from the ECMWF numerical weather prediction model. Trajectories of tracer particles are calculated using the mean winds interpolated from the analysis fields as well as random motion representing turbulence (Stohl and Thompson, 1999). For moist convective transport, FLEXPART uses the scheme of Emanuel and Živković Rothman (1999), as implemented and tested in FLEXPART by Forster et al. (2007a).

The particle trajectory calculations are done by integrating the trajectory equation

$$d\mathbf{X}/dt = \mathbf{v}[\mathbf{X}(t)] \tag{3.1}$$

where t is time, $\mathbf{X}$ the position vector and $\mathbf{v} = \overline{\mathbf{v}} + \mathbf{v_t} + \mathbf{v_m}$ the wind vector that is composed of the grid scale wind $\overline{\mathbf{v}}$, the turbulent wind fluctation $\mathbf{v_t}$ and the mesoscale wind fluctations $\mathbf{v_m}$.

The main advantage of FLEXPART is that it requires only a short computation time. The model was validated by Stohl et al. (1998) with data from continental-scale tracer experiments. In summary it seems to be one of the better dispersion models currently available. The model has been used in several studies on long-range atmospheric transport, and also on volcanic plumes (Eckhardt et al., 2008a; Prata et al., 2007).

3.1.1 Model setup

In this study the Lagrangian particle dispersion model FLEXPART is used to simulate the transport of sulphur dioxide (SO_2) emitted by a volcanic eruption. Simulations are carried out for a large number of emission altitudes above the volcano where particles are released and subsequently tracked in the model atmosphere.

The model simulations are based on meteorological analyses data provided by the European Centre for Medium-Range Weather Forecast (ECMWF, 2002). The ECMWF data have vertical resolution of 91 levels, and $1° \times 1°$ horizontal resolution. Analyses at 00:00, 06:00, 12:00 and 18:00 UTC as well as 3-h forecasts at intermediate times are used.

The first model setup is for the simulation used as input to the inversion method. This simulation explores the sensitivity of downwind SO_2 total columns to the altitude and mass of the initial emissions. The emissions are assumed to occur between ground and 25 km above the volcano. The total height is divided into 50 segments each 500 meters deep. Within every segment, 150 000 tracer particles with a total mass of 1 kg are released uniformly along a vertical line source. The simulation starts at the eruption onset which is assumed to take place 7 August 2008, at 22:30 UTC, based on reports from Alaska Volcano Observatory which indicate that satellite data show an ash plume in the vicinity of Kasatochi at this time. Even though the reports state that three explosive eruptions occurred between the late evening on 7 August and the early morning of 8 August, it is assumed that all mass is emitted at the eruption onset. The simulation extends for 3 days until 10 August 2008, at 22:30 UTC. The model computes concentrations every hour throughout the simulation. The output is on a $1° \times 1°$ grid, with 11 vertical layers. The lowest layer extends from ground up to 4 km above ground level (a.g.l) followed by 9 layers with vertical resolution of 2 km, and one single layer from 22-50 km a.g.l. Table 3.1 gives a summary of the model setup for the simulation used as input to the inversion method.

From this model simulation total atmospheric columns are computed, and since they are obtained with unit mass as source, they represent so-called source-receptor relationships. That means they describe the dispersion of tracers from their sources to different receptor locations in the atmosphere. The source-receptor matrices are used in the inversion method by comparing these modelled column quantities with total SO_2 columns retrieved from satellite measurements. The method determines the actual mass released at each level above the volcano.

Parameter	**Value**
Model	FLEXPART
Type of model	Lagrangian particle dispersion model
Coordinates of volcano	Latitude: 52.1693°N Longitude: 175.5113°W
Simulation start	07 August 2008, 22:30 UTC
Simulation end	10 August 2008, 22:30 UTC
Species released	Tracer
Release	Instantaneously at simulation start
Emission segments	0 - 50 km a.g.l
Depth of emission segments	500 m
Number of particles for each segment	150 000
Mass released for every segment	1 kg
Grid resolution	1° × 1°
Grid size	360° × 180°
Output time step	3600 s(60 min)
Output fields	Concentrations $[ng/m^3]$
Output layers	0-4km, 4-6km,...,22-50km

Table 3.1: *Modelling Input/Output Parameters for the simulation used as input to the inversion method.*

The inversion method will give an estimate of the height emission profile of SO_2. As elaborated in chapter 2, SO_2 is lost by e.g., reaction with OH as well as dry deposition. This first simulation which goes into the inversion only considers a tracer and no removal by dry deposition or reaction with OH. Since the lifetime of SO_2 in UTLS is of the order of a few weeks, the simulation extending over 3 days is assumed not to be critically sensitive to removal of SO_2. Nevertheless, at a later stage these removal processes were considered in the simulation, but did not give any noticeable effects on the height emission profile estimated by the inversion method.

After applying the inversion method and having obtained the so-called inversion profile (height emission profile), a longer simulation of the transport is performed. This model setup is quite similar to the previous simulation regarding horizontal output fields and simulation start. However, the 50 height segments are each given mass and particles according to the estimated height emission profile. The total number of particles released is increased to 4 million. The removal of SO_2 by dry deposition and reaction with OH are considered. The vertical output resolution is increased to 1 km, and further increased for comparison with LIDAR data. The simulation extends over one month following the eruption onset and is used for validation of the inversion profile.

A rather new feature in FLEXPART is the ability to compute removal by reaction with OH. Monthly averaged three-dimensional OH concentration fields are provided from the GEOS-CHEM model (Bey et al., 2001). If a positive value for the OH reaction rate is given, OH reaction is performed in the model simulation and tracer mass is lost by this reaction. A monthly averaged $3° \times 5°$ resolution OH field averaged to 7 atmospheric levels is used. The reaction rate is temperature corrected and an activation rate of 1000 J/mol is assumed (Eckhardt et al., 2008b). For these model simulations the OH reaction rate at 25°C is set to $k = 1.35 \times 10^{-12} cm^{-3} s^{-1}$, which gives a mean SO_2 lifetime of about 9 days when using a typical daytime OH concentration of 10^6 molecules cm^{-3} at the ground, and consider loss of SO_2 by OH only.

Dry deposition is described in FLEXPART by a deposition velocity

$$v_d(v) = -F_c/C(z) \tag{3.2}$$

where F_c and C are the flux and concentration of a species at height z within the constant flux layer. A constant deposition velocity v_d can be set. If the physical and chemical properties of a substance are known, more complex parametrisation for gases and particles are also possible (Eckhardt et al., 2008b). For this study, dry deposition of SO_2 was calculated with the resistance method (Wesely and Hicks, 1977) using data from Wesely (1989) with updates.

Since SO_2 is only slightly soluble, wet deposition is of minor importance and was not considered as a sink for SO_2. Berglen et al. (2004) calculated loss of SO_2 by wet deposition in the troposphere to 1.7% of the total loss of SO_2, using the OsloCTM2 model. However, SO_2 in the troposphere is also lost by aqueous oxidation by O_3, H_2O_2 and HO_2NO_2, the latter one being of minor importance. None of these aqueous removal processes were considered in the model simulation, nor was catalytic decay of SO_2 by metals which also is rather important (Berglen et al., 2004).

3.2 Satellite data

Several satellite instruments were able to make measurements of the eruption of Kasatochi Volcano on 7 August 2008 and also the days following the eruption. This subsection will give an overview of the satellite data used in this study. First, satellite instruments in general are discussed, thereafter the specific instruments used in this study are introduced.

There are several important sensors aboard a group of satellites termed the Afternoon Constellation, or NASAs A-Train, for short. The name is due to the local afternoon overpass time. The constellation consists of several polar-orbiting satellites in close formation. NASA's Aqua satellite is leading the A-train, followed by CloudSat, CALIPSO, the European PARASOL satellite, and NASA's Aura satellite. The local times (LT) of overpass by the satellites starts at 01:30 PM, and the last satellite overpasses at 01:38 PM LT. The result is that the same air mass is observed by multiple instruments within a 15-min time window.

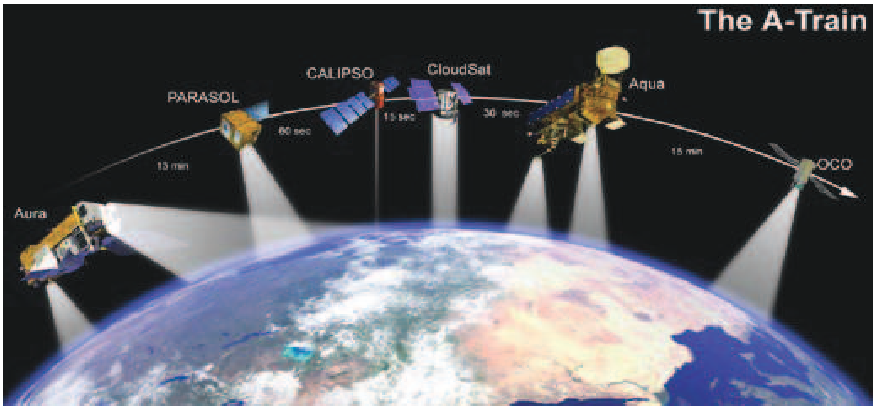

Figure 3.1: *NASA's A-train spacecraft. Source: NASA (2008)*

The instruments can in general be used to measure clouds, moisture, aerosols, gases etc in the atmosphere. Of special interest are the sensors which can be used to detect and track volcanic emissions, especially SO_2. These types of instruments on the Aura Platform are the Ozone Monitoring Instrument (OMI), Microwave Limb Sounder (MLS) and Tropospheric Emission Spectrometer (TES). On the Aqua platform, Atmospheric Infrared Sounder (AIRS) and Moderate Resolution Infrared Spectroradiometer (MODIS) can also measure SO_2 of volcanic origin. Also of special interest is the Cloud-Aerosol Lidar with Orthogonal Polarization (CALIOP) on board the CALIPSO satellite, which can measure cloud height and aerosol type. The instruments utilised in this study are AIRS and OMI.

In general, the retrievals of SO_2 column abundances from the satellite instruments are based on making use of radiation at specific wavenumbers that is affected by absorption of a specific gas in the atmosphere. For the infrared (IR) radiation measured by AIRS, SO_2 has absorption features at 4, 7.3 and 8.6 μm. For ultraviolet (UV) radiation, measured by OMI, SO_2 has significant absorption structures in the spectral region between 310 and 340 nm.

3.2.1 AIRS

The Atmospheric Infra-Red Sounder - AIRS on board the EOS-Aqua polar orbiting satellite was able to track the SO_2 cloud from Kasatochi for more than two weeks as the cloud moved over Europe and on to Russia. The instrument has high spectral resolution and is operating at infrared wavelengths between 3.7 and 15.4μm (Chahine et al., 2006). One big advantage with this instrument is the ability to make observations during nighttime since the instrument makes use of infrared radiation.

Satellite infrared retrievals based on the AIRS measurements were made available for the eruption of Kasatochi by Fred Prata at NILU. No vertical resolution of SO_2 can be obtained by the satellite, but total SO_2 column abundances were determined by use of the retrieval scheme developed by Prata and Bernardo (2007). The algorithms for determining SO_2 from AIRS exploit the strong SO_2 anti-symmetric absorption feature near 7.3 μm, but because water vapour also absorbs strongly across this band, the retrievals are restricted to UTLS - the upper troposphere (heights $>$ 3 km) and lower stratosphere. For more details on the retrieval, see Prata and Bernardo (2007). Some of the observations are incomplete, meaning that the swath width of the instrument was insufficiently wide in order to capture the complete cloud, as seen on the east side of the plume of figure 3.2(a), with the swath width boundaries marked with grey lines. Maximum UTLS mass loadings were found to be $\sim$1.2 Tg from this instrument, this is slightly lower than that found using ultra-violet OMI measurements. The difference is mostly due to the lower penetration depth of the AIRS measurements.

The satellite data were made available in non-gridded text format on specific longitudes and latitudes with values of SO_2 in Dobson Unit (DU). The data were subsequently resampled to a grid of the same size as the FLEXPART output data, that is a global grid of $1^\circ \times 1^\circ$. The instrument made observations of the Kasatochi plume at times between 11:30 and 14:30, and 21:30 and 00:30 (all times in UTC). For input to the inversion method the satellite data were approximated to the nearest hour to be compared with the corresponding time of the FLEXPART simulation. Table 3.2 gives an overview of the observations used in the inversion method.

Date	Approximate time	Actual time
08.08	13:30 UTC	13:42 UTC
08.08	23:30 UTC	23:11 UTC
09.08	00:30 UTC	00:53 UTC
09.08	12:30 UTC	12:41 UTC
09.08	14:30 UTC	14:23 UTC
09.08	22:30 UTC	22:17 UTC
09.08	23:30 UTC	23:53 UTC
10.08	11:30 UTC	11:53 UTC
10.08	13:30 UTC	13:29 UTC
10.08	21:30 UTC	21:23 UTC

Table 3.2: *AIRS observation times used as input to the inversion method.*

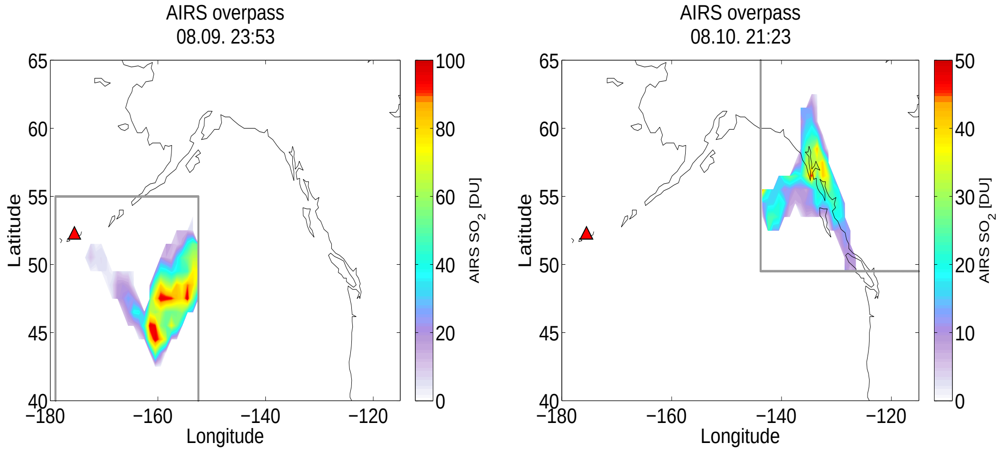

(a) (b)

Figure 3.2: *SO_2 columns measured by the AIRS instrument on a) 9 August at 23:53 UTC and b) 10 August at 21:23 UTC. The swath width boundaries of the overpasses are marked with grey lines.*

3.2.2 OMI

The Ozone monitoring instrument - OMI is a Dutch-Finnish instrument and was provided to the EOS/Aura mission by the Netherlands and Finland. The instrument was designed principally for measuring global ozone. It measures solar back-scattered radiation in the UV between 270 and 365 nm, thus, no observations are available after sunset or at low solar elevation. In the days that followed the eruption of Kasatochi, the OMI instrument tracked a dense cloud of sulphur dioxide dispersing over The Pacific Ocean as shown in figure 3.3.

Satellite retrievals of SO_2 column abundances based on the OMI measurements were made available for the eruption of Kasatochi by Fred Prata at NILU and are based on retrieval schemes described by Krotkov et al. (2006) and Yang et al. (2007). The algorithm used for determining SO_2 from OMI exploit SO_2 absorption features between 310 and 340 nm. The challenge is to distinguish SO_2 absorption effects from those of ozone which absorbs in the same spectral region. This absorption effect has been accounted for in the algorithm. Maximum SO_2 mass loadings were found to be $\sim$1.3 Tg from OMI.

The satellite data were made available in gridded format on a 1°×1°grid from 180°E to 180°W, and 40°N to 85°N. Values were given as SO_2 column data in Dobson Unit (DU). Usually there were 14 or 15 scenes (orbits) in a day, which is typical for a polar orbiter. The scenes and times (given in seconds after 00UTC) which covered the Kasatochi plume were identified and used. For input to the inversion method the satellite data were approximated to the nearest hour to be compared with the corresponding time of the FLEXPART simulation. Table 3.3 gives an overview of the observations used in the inversion method.

Date	**Approximate time**	**Actual time**
08.08	23:30 UTC	23:30 UTC
10.08	00:30 UTC	00:13 UTC

Table 3.3: *OMI observation times used as input to the inversion method.*

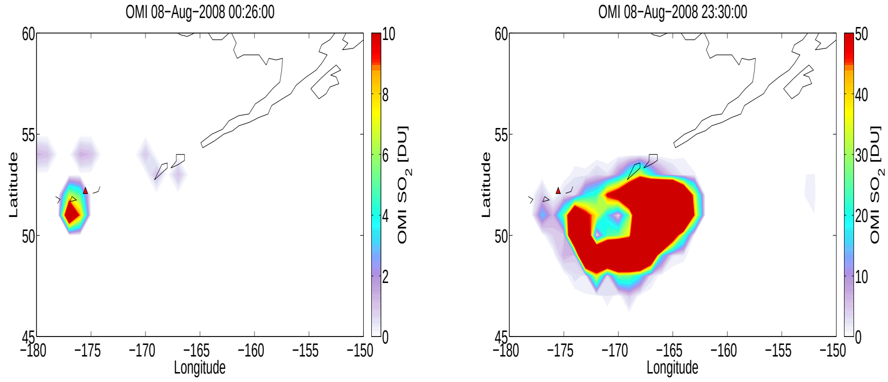

(a) (b)

Figure 3.3: *SO_2 columns measured by the OMI instrument on a) 8 August at 00:26 UTC and b) 8 August at 23:30 UTC.*

3.2.3 Weighting function

The satellite retrievals have a significant dependence on the height of the observed SO_2 cloud. For gases, such as SO_2, which is not uniformly distributed in the atmosphere, an assumption has to be made about the height of the SO_2 cloud. The assumption comprises contributions to total column quantities from certain height intervals. Consequently, the satellite measurements do not give actual total column quantities, rather a "weighted" total column. For infrared satellite retrievals, the weighting functions depend mainly on the temperature profile of the atmosphere. The SO_2 molecules vibrate in a certain way giving their temperature and signal. In addition, the satellite receives a signal from the environmental atmosphere. This means that the satellite can receive the exact same signal from one height level containing a certain amount of SO_2 and another height level with different environmental temperature containing a different amount of SO_2, resulting in errors in the retrieval of column abundances. Some sort of constraint has to be set on the signal depending on the assumed height of the SO_2 cloud.

The upwelling radiance I_v at wavenumber v at the top of the atmosphere and potentially reaching the satellite is defined by the radiative transfer equation as

$$I_v = \int_0^{\infty} B_v[T(z)] \frac{d\tau_v(q,z)}{dz} dz \tag{3.3}$$

where B is the Planck function, in principle saying that emitted intensity of an object increases with temperature and that the wavenumber of the maximum intensity increases with increasing temperature. τ is the transmittance, meaning the fraction of radiation at a specified wavenumber v that passes through the atmosphere. q is the absorber profile of the atmosphere and z is the height level.

The weighting function is defined by

$$W = \frac{d\tau_v(q,z)}{dz} \tag{3.4}$$

For example, one weighting function can imply that the strongest SO_2-signal is found at the height level around 15 km and the signal is decreasing toward lower and higher altitudes. Near ground level the weighting function can be close to zero which means that if there is SO_2 present, the satellite can not observe it.

Usually the weighting function is calculated using a radiative transfer model to calculate the absorber profile and transmittance. Also an analytical function can be used as an approximation. In summary the weighting function represents the contribution from a layer located at height level z to the radiance sensed by the satellite. This provides information on what regions of the atmosphere affect satellite measurements.

Figure 3.4 gives examples of different weighting functions and related transmittances for a radiometer on board the NOAA 2 satellite, an early atmospheric sounding instrument. The numbers indicate different channels or set of wavenumbers. The figure shows that some channels receive no radiation from the surface ($\tau \rightarrow 0, W \rightarrow 0$).

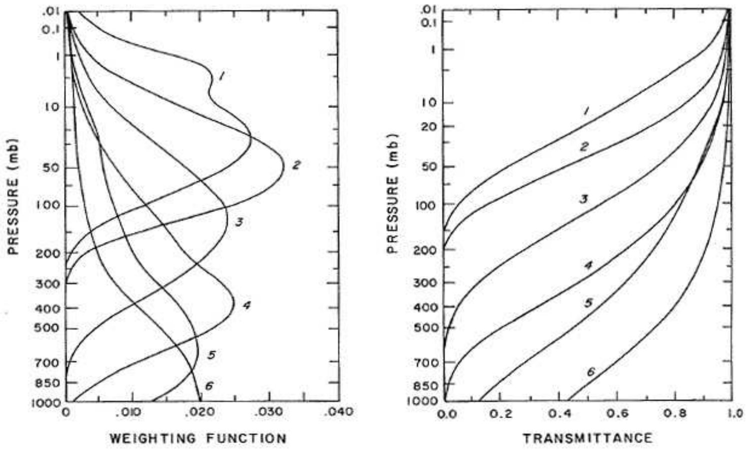

Figure 3.4: *Weighting function and transmittance. From: Liou (2002).*

The infrared SO_2 retrievals from the AIRS instrument are restricted to the UTLS, while the OMI instrument, measuring in the UV region, provides total column SO_2 measurements. The OMI UV retrievals also have a sensitivity to the height of the SO_2 as explained by Yang et al. (2007). When using satellite data for input to the inversion method, total atmospheric columns from the FLEXPART simulation were calculated by weighting the concentrations in the output layers with the respective weighting function shown in figure 3.5.

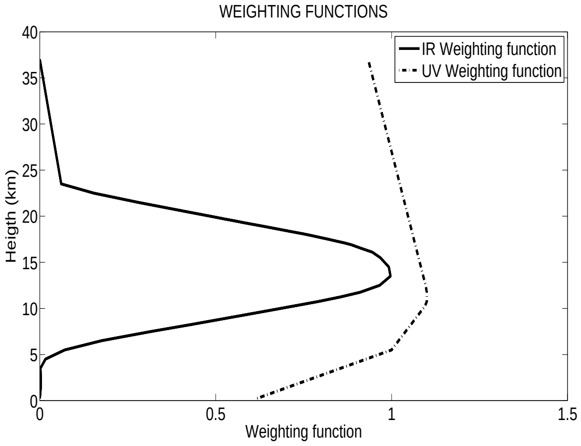

Figure 3.5: *Infrared (AIRS) weighting function for a channel containing an atmospheric SO_2 layer near 15 km, and UV (OMI) weighting function for a clear atmosphere, adapted from figure 7 of Yang et al. (2007).*

The weighting function is further explored in the results chapter by using an analytical weighting function. This function is described by the dimensionless transmittance function

$$\tau = \exp\left[-\frac{k}{f}u_0(e^{-z} - e^{-z_T}) - ku_1z_0(1 + \frac{z}{z_0})e^{-\frac{z}{z_0}} - (1 + \frac{z_T}{z_0})e^{-\frac{z_T}{z_0}}\right] \quad (3.5)$$

where z_0 is the height where the absorber profile peaks, u_0 the total column abundance, u_1 an inversion parameter, k the absorption coefficient, zz is defined as z/z_0, zT defined as z_{max} and $f = 1 + z_0u_1/u_0$. Sensitivity studies of the effect of the weighting function on the inversion profile are carried out.

3.3 Inversion method

The analytical inversion method used in this study is based on work of Seibert (2000) and has been described in a recent publication of Eckhardt et al. (2008a). The mathematical theory of the method is based on simple linear algebra. This section will first describe the method from a physical perspective before introducing the fundamental mathematical equations of the method.

The general idea of the method is to use measurements of atmospheric trace constituents together with source-receptor relationships obtained by dispersion model calculations, to determine the sources of the trace substances. In this study the inversion problem is solved to give an estimation of the vertical SO_2 emission profile (SO_2 sources) of a volcanic eruption. This is done by using observed total SO_2 column abundances from satellite measurements (OMI, AIRS) and modelled total SO_2 columns from an atmospheric dispersion model (FLEXPART).

The physical aspect of the inversion method uses the fact that winds normally change with altitude and thus the position and shape of the plume are determined by the altitude of the emissions. That is, because of the vertical wind shear and different flow regimes at different altitudes, the plume shapes will generally be very different for emissions at different altitudes. For instance, mass emitted low in the atmosphere will generally be transported rather slowly, whereas mass emitted into the jet stream will be quickly transported away from the volcano. Using a dispersion model to simulate the emissions by releasing a unit amount of SO_2 at a large number of stacked height levels, it is possible to examine the sensitivity of the shape of the simulated plume to changes in the height of the initial eruptive injection into the atmosphere. Satellite observations of the plume position and shape can be used to put a tight constraint on the possible altitude of the injection.

In past studies, e.g., Carn et al. (2007, 2008a,b); Prata and Bernardo (2007); Prata et al. (2007); Prata and Kerkmann (2007); Schneider et al. (1999), researchers have sometimes qualitatively compared observed plumes with multiple simulations of different emission heights, in order to pick the "best" simulation and, thus infer the initial emission altitude. However, as plume shapes can become quite complex even after only a few days of transport and subjective comparisons can be difficult to make or even misleading, a more objective method is needed. Furthermore, the emission will usually not occur at one discrete height only. Instead, the emission height profile can be quite complex, with emissions occurring at multiple altitudes.

The aim of the inversion method is to seek a linear combination of the plumes resulting from various simulations that best fits the observations, i.e., minimises the difference between observed and modelled values. More specific, this is done by comparing observed and modelled total column values of SO_2. The model-derived total SO_2 columns are calculated assuming that the emissions occurred within a vertical column above the volcano extending from ground up to a specified altitude. This column is divided into a number of elements, which in this study is a total of fifty elements. For each element, particles with a total mass of 1 kg are released and tracked as they disperse with the winds. Each of these release elements represents a single model simulation, this means for each release element concentrations and total columns are calculated every hour after the eruption onset. Consequently, after one hour, fifty SO_2 columns are calculated for each grid point, each one representing a release from a distinct height level. Since each release element contains a unit mass as source, these model-derived column values represent so-called source-receptor relationships, which means that the model simulations explore the sensitivity of the downwind total SO_2 columns to the emitted mass at every altitude. Subsequently, one and each of the model-derived columns are compared to the observed SO_2 columns to find the best fit to the observations. The release heights of the modelled columns that are a best match to the observed columns can be identified, resulting in an estimate on the source profile. Since unit masses have been released for the various model simulations, the scaling factors with which the different simulations are weighted will reflect the masses to be released at these heights in order to best fit the observations.

One problem that frequently occurs with inverse methods is that the constraints posed by the observations are ill-posed, and this can lead to spurious solutions, i.e. unrealistic height profiles in this case. Small errors in the observations or in the model results can thereby cause disproportionally large errors in the inverted emission profile. For example, imagine a volcanic eruption that emits SO_2 at low altitudes and thus at the time of an observation shortly after, the plume is still in the vicinity of the source. However, if there is some other observation of SO_2 further away from the volcano which in reality does not originate from the volcanic eruption of consideration (this could be due to a measurement error or to another, probably industrial, SO_2 source), the inversion method will try to fit this observation by releasing mass at any altitude that would allow fitting this observation, probably at a high altitude to allow for fast transport to the far-away observation location. Especially if the simulated plume has low total column values at this position for all altitudes (i.e., a small value of the source-receptor relationship), the algorithm will try to compensate for this by releasing a large mass in order to fit the observation, unless this leads to bad agreement with other observations. Furthermore, in the extreme case that not a single observation constrains a particular model simulation (for instance, the simulated plume for a high-altitude release has moved out of the observation domain), there is no constraint at all on the emitted mass at this altitude and, thus an inversion constrained only by the observations can produce any mass released at this altitude. Moreover, problems can arise from areas where there are several opportunities of match between the satellite observations and the model simulations, so that a large number of (probably very different) solutions can be obtained at relatively similar "costs" (i.e., overall model-measurement misfit).

To remedy this situation, additional information is necessary to obtain a meaningful solution. The additional information is provided in the form of *a priori* information for the unknown source profile. A priori information refers to prior knowledge about the source distribution. This is a widely used term in statistical analysis. The a priori can be determined based on indications on the emission height profile by other observations. If no reports on the emissions are known beforehand, a constant and even a zero a priori (so-called Tikhonov regularization) can be used.

The method also considers the uncertainties of the a priori profile and of the observations (including the model error), which are to be specified for each application. The effect of the a priori uncertainties is to constrain the solution with the a priori information, thus if the a priori uncertainties are low, the solution profile will mainly be determined by the a priori profile, that is, the solution (source profile) will follow the a priori profile closely. Similarly, low uncertainties for the observations cause the solution profile to be determined mainly by the observations. The uncertainties in the a priori and uncertainties in the observations "weigh" the influence of the a priori against the measurement-model misfit, so the important consideration is the ratio between the two uncertainties mentioned above. A balance must be obtained between the two in order to achieve a reasonable solution profile. Currently, the practice is to determine this ratio by trial-and-error fits between the two uncertainties. However, in principle one should have some statistical information for instance on the standard errors of the model-observation misfit.

Moreover, a condition on the smoothness of the solution, as well as an iterative algorithm for removing unphysical negative values arising from inaccuracies in the model and data, are included in the inversion method to yield a meaningful solution.

The mathematical theory of the inversion method includes

- $\boldsymbol{x}$: The n=50 unknowns, giving the height emission profile (solution or source vector) we want to retrieve.
- $\boldsymbol{x^a}$: The a priori profile of emitted masses.
- $\boldsymbol{y^o}$: The m observed values (i.e., total SO_2 columns) from the satellite data, the subscript $\boldsymbol{o}$ meaning observations.
- $\boldsymbol{M}$: The modelled sensitivities of the m SO_2 total columns to the n source terms, calculated by the FLEXPART simulation (so-called source-receptor relationship), a $m \times n$ matrix.

The modelled values $\boldsymbol{y}$ corresponding to the observed values $\boldsymbol{y^o}$ can be found by applying the calculated source-receptor relationship $\boldsymbol{M}$ to the solution vector $\boldsymbol{x}$

$$\mathbf{y} = \mathbf{Mx} \tag{3.6}$$

This equation can not be solved directly for $\boldsymbol{x}$ because the problem is ill-conditioned. Additional information (regularization) is necessary to obtain a meaningful solution. Tikhonov regularization constrains the solution by requiring the solution to be minimised, thus requiring that the square length of the solution vector $||x||^2$ is small. This means that large (and often spurious) emitted masses is constrained by creating a "penalty" to them. Large masses are only accepted if they are supported by the measurements, and not only to satisfy one single observation. Implicitly this means zero a priori values. Introducing an explicit a priori vector $\boldsymbol{x^a}$, we can write

$$\mathbf{M}(\mathbf{x} - \mathbf{x^a}) \approx \mathbf{y^o} - \mathbf{Mx^a} \tag{3.7}$$

It is convenient to write the above equation as an abbreviation like

$$\mathbf{M}\tilde{\mathbf{x}} \approx \tilde{\mathbf{y}} \tag{3.8}$$

The above equation includes the observation vector, $\boldsymbol{y^o}$, and the source vector, $\boldsymbol{x}$. Together with the matrix, $\boldsymbol{M}$, these parameters make up the basic equation of the inversion method. It is not an exactly fulfilled equation. We want to make the disagreement between the left hand side (LHS) and the right hand side (RHS) as small as possible. Thus the goal is to find an estimation of the source vector which should, when the source-receptor matrix is applied to it, reproduce the observation vector as well as possible while at the same time resulting in minimal deviation from the a priori.

The further mathematical framework of the inversion method yields minimising a cost function J. The cost function results from rearrangement of equation 3.8. The disagreement between the LHS and the RHS is the cost function. The equation is made "exact" by introducing a "misfit" (i.e., cost) term. The cost function J consists of three terms, $J = J_1 + J_2 + J_3$

$$\begin{aligned} J_1 &= \sigma_o^{-2}(\mathbf{M}\tilde{\mathbf{x}} - \tilde{\mathbf{y}})^{\mathbf{T}}(\mathbf{M}\tilde{\mathbf{x}} - \tilde{\mathbf{y}}) \\ J_2 &= \tilde{\mathbf{x}}^T\mathbf{diag}(\sigma_{\mathbf{x}}{}^{-\mathbf{2}})\tilde{\mathbf{x}} \\ J_3 &= \epsilon(\mathbf{D}\tilde{\mathbf{x}})^T\mathbf{D}\tilde{\mathbf{x}} \end{aligned} \tag{3.9}$$

J_1 measures the misfit between model and observation. J_2 is the deviation from the a priori values, and J_3 the deviation from smoothness. σ_o is the standard error (uncertainties) of the observations, and $\sigma_{\mathbf{x}}$ is the vector of standard errors (uncertainties) of the a priori values. ϵ determines the smoothness condition and $\boldsymbol{D}$ represents the second derivative.

Minimisation of J leads to a linear system of equation (Eq. 3.10) which is to be solved for $\tilde{\mathbf{x}}$ with a linear algebra package routine called SGESVX.

$$[\sigma_o^{-2}\mathbf{M^T M} + \mathbf{diag}(\sigma_{\mathbf{x}}{}^{-\mathbf{2}}) + \epsilon\mathbf{D^T D}]\tilde{\mathbf{x}} = \sigma_{\mathbf{o}}^{-\mathbf{2}}\mathbf{M^T}\tilde{\mathbf{y}} \tag{3.10}$$

For this study, different scenarios for the a priori $\mathbf{x_a}$ are tested, including a constant and non-constant a priori profile. The a priori uncertainties, $\sigma_{\mathbf{x}}$, are specified for each source element as a vector. The magnitude of the uncertainties was chosen to allow substantial corrections to the initial profile.

The standard errors of the observations, σ_o, should ideally be specified for each receptor element and should contain not only the measurement error but rather a standard misfit between the observations and the model results. Because of lacking detailed information, the actual measurement uncertainty is used for the AIRS observations with σ_o= 3 DU, which assumes that the large measurement uncertainty will dominate the measurement-model misfit. For OMI, the standard error is chosen to allow for some variable biases in the OMI retrieval as well as errors from the model simulations, giving σ_o = 2 DU for the OMI measurements.

The inversion method is applied in the form of an executable fortran program which calculates and minimises the cost function.

3.3.1 Previous case study

Eckhardt et al. (2008a) used the inversion method in a study of the eruption of the Jebel at Tair volcano (15.55°N, 41.83°E) located in the Red Sea. The eruption occurred 30 September 2007 around 11-11:30 UTC, and injected approximately 80 kilotons (kt) of SO_2 into the atmosphere. Several satellites were able to detect SO_2 from the eruption including AIRS and OMI, and especially encouraging was the use of the SEVIRI instrument. The short time resolution (15 min) of this instrument makes it very encouraging for operational use with the inversion method. The Lagrangian dispersion model FLEXPART was used to calculate source-receptor relationships used in the inversion method.

Figure 3.6 shows the inversion results for this case study. Emission maxima are located at about 16 km a.s.l, and near 5, 9, 12 and 14 km. Data from a single platform (either AIRS, OMI or SEVIRI alone) would have sufficed to produce an emission profile in good agreement with the reference profile (using data from all three platforms). Even using SEVIRI data only from 10-15 hours after the eruption gave comparable results. Sensitivity experiments showed that the results were robust against changes in the a priori profile, including a zero a priori emission profile. Validation against independent OMI data, and comparison with vertical profiles of aerosol backscatter retrieved from a space-based LIDAR (CALIPSO), showed very good agreement with the FLEXPART simulation using the emission profile from the reference inversion. The plume dispersion could be simulated well for several days after the eruption.

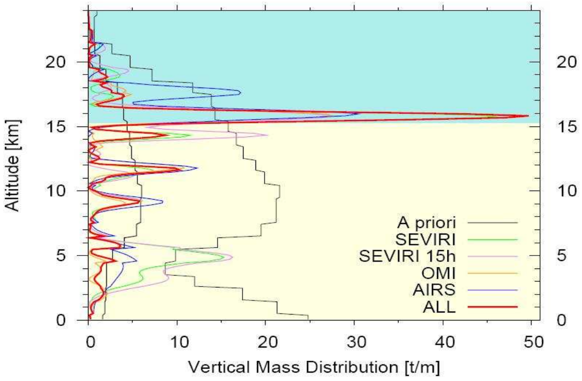

Figure 3.6: *Inversion results for Jebel At Tair, 30 September 2007. The coloured lines represent inversion results using different satellite data. The red line is called the "reference case". The thick black line shows the a priori profile, the thin black line its assumed uncertainty. Source: Eckhardt et al. (2008a).*

3.4 LIDAR measurements

LIDAR (Light Detection and Ranging) is an optical remote sensing technology that measures properties of scattered light to find range and other information of a distant target. The general method makes use of laser pulses to determine properties of an 'object', e.g. sulphate particles in the atmosphere. The particles cause an enhanced backscatter which the LIDAR is capable of measuring. From the LIDAR measurements we can retrieve aerosol extinction profiles, which is a measure of attenuation of the light passing through the atmosphere due to the scattering and absorption by aerosol particles. By definition the extinction coefficient is the fractional depletion of radiance per unit path length, and has units of km^{-1} .

In this thesis, the aerosol extinction coefficient is used as a qualitative measure of the sulphate concentrations in the atmosphere and is compared with the SO_2 concentration simulated by FLEXPART. Aerosol extinction coefficient and concentration of SO_2 are two very different quantities. However, the comparison is used only in a qualitative manner to evaluate the altitude of the simulated plume.

3.4.1 Nova Scotia

The Dalhousie Raman LIDAR at Nova Scotia, Halifax (44.6° N, 63.6° W) on the eastern coast of Canada, was able to observe the Kasatochi plume. The location of the ground based LIDAR is marked by a green circle in center of the figures 4.7 and 4.8 in the results chapter. The measurements of the plume were available from 21 August 2008 and the days following. Figures of the measurements were prepared by Lubna Bitar at Dalhousie University.

3.4.2 Ny Ålesund

Koldewey station, operated by AWI (Alfred-Wegener-Institut für Polar- und Meeresforschung) in Ny Ålesund (78.9° N, 11.9° E) on Svalbard, was also able to observe the Kasatochi plume using a ground based LIDAR. One major part of the scientific work at Koldewey Station is the observation of the north polar stratosphere. Several optical instruments are installed and operated, including a LIDAR determining the concentration of ozone and aerosols in the atmosphere. The LIDAR measurements of the Kasatochi plume were taken from 15 August 2008 to 5 September 2008. Several layers were observed at about 10-17 km altitude. It is not evident that all of these layers originate from the eruption of Kasatochi, comparison with FLEXPART simulation will prove if they are, and allow for evaluation of the estimated height profile. The observations were provided by AWI (pers. comm.).

Chapter 4

Results and discussion

In this section the SO_2 inversion results for the Kasatochi eruption are presented before a comparison with independent height emission profiles for the eruption is given. A consistency check is performed and thereafter the transport of the volcanic SO_2 plume with emissions according to the inversion profile is illustrated, and also a comparison with an uniform emission height profile is given. Subsequently, the estimated emission height profile is validated, before several sensitivity studies for the inversion profile are given. Eventually the SO_2 decay by reaction with OH and by dry deposition in the model simulation are explored.

4.1 Inversion results

Satellite data for up to 72 hours after the eruption were used in the inversion method for this case study. For aviation purposes, the time-critical part involves using satellite data from only the first day after the eruption (or even less). However, in this case study, there were not enough data available for the first day after the eruption and it was therefore chosen to use data for up to 72 hours after the eruption. Later on, sensitivity studies were carried out regarding the amount of satellite data used in the inversion method. For less time critical applications, such as determining the injection altitude for the purpose of climate modelling, later satellite data can be accepted. Still, precautions have to be made about using satellite data for too long after the eruption as this can yield errors from e.g., chemical transformations and removal by SO_2.

4.1.1 AIRS data

AIRS data from 72 hours after the eruption were used for the so-called "default" inversion. During these hours, a total of 10 applicable observations of the Kasatochi SO_2 plume were available and are listed in table 3.2. In addition, the IR weighting function showed in figure 3.5 was used to weigh the FLEXPART data used in the inversion method. Both a constant a priori profile and a non constant a priori were applied. The total mass of both the a priori profiles was specified to 1.3 Mt, which is in agreement with the AIRS and the OMI emission estimates.

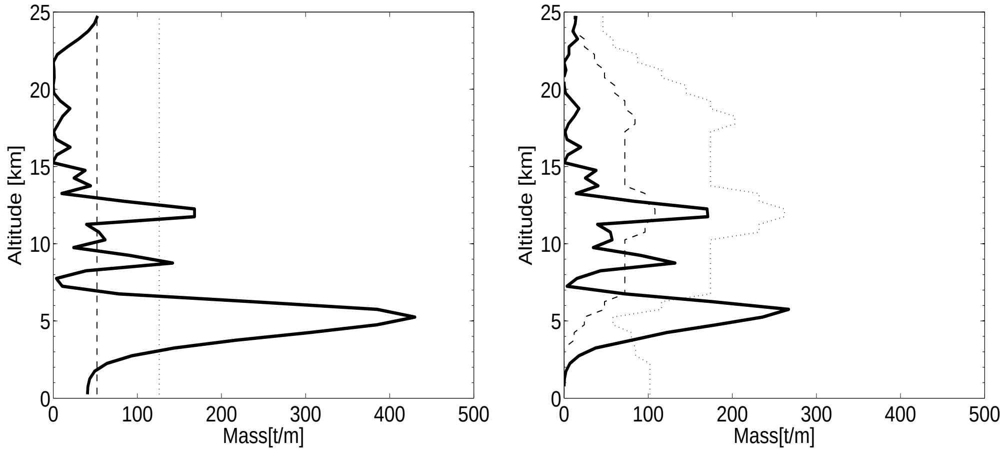

(a) Constant a priori

(b) Non constant a priori

Figure 4.1: *Inversion results when using AIRS data from 72 hours after the eruption. The solid line shows the inversion profile of SO_2 in tons/meter. The dashed line is the a priori profile, the dotted line its assumed uncertainty.*

The results from the default inversion are shown in figure 4.1. The inversion profiles, also called the a posteriories, show a strong SO_2 emission peak at ~5 km, and secondary peaks at ~9 km and ~12 km, with large emissions also between these two peaks. Smaller peaks are found at ~14 km, ~16 km and ~18 km.

Consider first the constant a priori inversion shown in figure 4.1(a). In addition to the emissions below 20 km, there are also large emissions above 22 km. However, these emissions follow the a priori, thus are bounded by the a priori profile at these heights. Similarly, the emissions from 1-2 km height follow the a priori closely. Furthermore, the emission peak around 5 km is very high and probably quite uncertain (this emission peak is discussed in more detail later). The total mass of this inversion profile is on the order of ∼1.9 Mt which exceeds the total a priori mass of 1.3 Mt by ∼45%.

Figure 4.1(b) shows the inversion profile using the non constant a priori profile. This a priori profile was determined on the basis of a test case using an emission peak at around 12 km, and also to constrain the assumed unphysical increase in mass above 22 km, as well as the very high emission peak around 5 km. The a priori values and the a priori uncertainties were lowered for the height levels containing these emissions, thus the emissions are reduced here. With this a priori the total mass of the a posteriori is on the order of ∼1.2 Mt which is a closer match to the a priori mass of 1.3 Mt.

Also for the non constant a priori, the a posteriori above 22 km, as well as the emissions below 2-3 km are bounded by the a priori. For these heights, the solutions for the a posteriori are very different for the cases using constant and non constant a priori. Both solutions follow the a priori closely at these height levels which imply that that the satellite data do not provide any constraint on these parts of the profile. It is seen that the emissions from 20-22 km are well constrained, as these emissions are not bounded by the a priori in either of the cases. The emissions below 1-2 km and above 22 km is poorly constrained. This is also what the infrared weighting function on figure 3.5 suggests, with very low sensitivity below 5 km and quite low sensitivity above 22 km. This means that AIRS does not observe the SO_2 below 4-5 km, and only poorly observe the SO_2 above 22 km.

So, regardless of which a priori that is used, the a posteriori above 22 km closely follow the a priori and thus the measurements obviously do not provide constraints for these emissions. Possibly at these heights, the plume moves into a different direction, so that there are no observations in this region that could prove the a priori wrong. Additional data, e.g. observations close to zero from another overpass, could constrain these observations. However, by investigating this more closely, it was found that these emissions hardly move at all but stay above the volcano during the days following the eruption (this can be seen on the figures 4.7 and 4.8 later in this chapter). Additional data to constrain these emissions was not available therefore the non constant a priori was chosen in order to reduce the emissions by changing the a priori above 20 km.

Comparing the inversion profiles of both the constant and the non constant a priori, it is clear that the inversion method is relatively robust against changes in the a priori profile. For the remainder of the study, considering simulation of the transport of the volcanic emissions etc., the inversion profile using the non constant a priori was used.

4.1.2 OMI data

OMI data from 50 hours after the eruption were used for the OMI inversions. During the first 50 hours, only two applicable observations of the Kasatochi SO_2 plume were available and are listed in table 3.3. This might be an insufficient amount of satellite data, however it was chosen to make an inversion to see if the result was comparable to the AIRS inversions. The UV weighting function from figure 3.5 were applied to the FLEXPART data used in the inversion method. The same constant a priori profile and a non constant a priori as used with the AIRS data were employed.

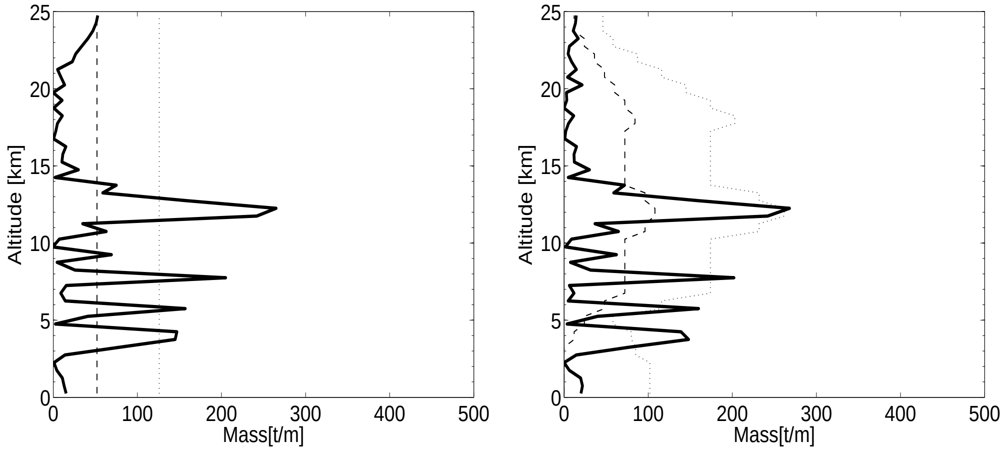

(a) Constant a priori (b) Non constant a priori

Figure 4.2: *Inversion results when using OMI data from 50 hours after the eruption. The solid line shows the inversion profile of SO_2 in tons/meter. The dashed line is the a priori profile, the dotted line its assumed uncertainty.*

The results from the OMI inversions are shown in figure 4.2. The inversion profiles show SO_2 emission peaks at ∼4 km, ∼6 km, ∼8 km and ∼12 km. Smaller emissions are found at ∼9 km, ∼15 km and ∼18 km. The total mass of the a posteriori using the non constant a priori, is on the order of ∼1.0 Mt.

Compared to the AIRS inversion profiles there are several similarities. The most prominent is the emission peak at around 12 km which is also estimated by using AIRS data, however the peak is intensified using OMI data. The emissions below 10 km are quite similar except for more peaks occurring when using OMI data. The large emission peak around 5 km found by using AIRS data is strongly reduced when using OMI data and the peak is divided into two peaks at 4 and 6 km. Furthermore, AIRS data resulted in an emission peak around 9 km, which is also estimated by OMI data, however there is a stronger peak at 8 km. Above 15 km there are smaller emissions also estimated by using AIRS data. Considering the emissions above 22 km, the OMI measurements, similar to the AIRS data, obviously do not provide any constraint for these high altitude emissions as these emissions follow the a apriori closely regardless of which a priori is used.

The OMI satellite data are not restricted to the UTLS like AIRS, which means that if there is SO_2 present in the lower troposphere, OMI is able to observe it to some extent. Therefore, the lower emissions estimated by using OMI data are likely to be more accurate than when using AIRS data. The fact that OMI data does not estimate large emissions at 5 km, strengthen the presumptions of the high uncertainties of these emissions using AIRS data.

For the OMI inversion profile using the non constant a priori, the mass of the profile below 10 km is about 0.49 Mt. Compared to the respective AIRS inversion profile, with a mass of about 0.75 Mt below 10 km, the use of OMI data clearly reduce the tropospheric SO_2 emissions. Above 10 km (roughly in the lower stratosphere as the tropopause where found at $\sim$10 km) the mass of the OMI inversion profile is about 0.56 Mt, and is more similar to the AIRS mass of 0.42 Mt. Both AIRS and OMI inversions yield emissions of SO_2 into the stratosphere which potentially can give a climatic effect. In summary, for the AIRS inversion approximately 36% of the mass of SO_2 was injected above the tropopause, while for the OMI inversion 54% of the SO_2 reach the lower stratosphere.

4.2 Height profiles from independent studies

Maerker et al. (2008) used a trajectory matching technique, as described in the introduction chapter, based on FLEXPART simulations and GOME-2 satellite SO_2 observations, to estimate the SO_2 height emission profile of the Kasatochi eruption. Figure 4.3 shows the estimated height emission profile obtained by their method. The 8-9 km and 12-14 km peaks are in agreement with the respective peaks in the inversion profiles.

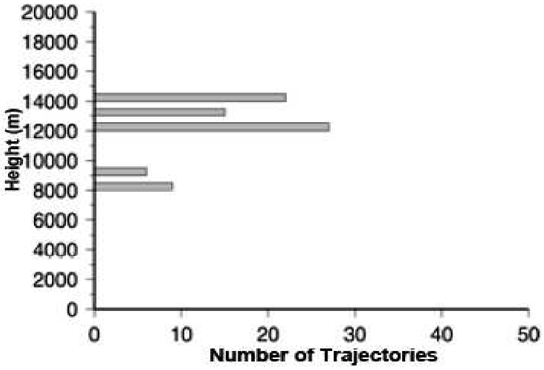

Figure 4.3: *Estimated emission height of the Kasatochi eruption 7 August 2008. From Maerker et al. (2008).*

Theys et al. (2009) detected volcanic bromine monoxide (BrO) emissions from the Kasatochi eruption using the GOME-2 satellite instrument, and also used FLEXPART to simulate the dispersion of the plume. By using a BrO tracer and assuming various initial plume heights varying between 2 and 24 km altitude, they performed a series of FLEXPART simulations which subsequently were compared to the observed BrO to infer information about the altitude of the BrO emissions. So correlation coefficients were calculated to give the best fit between the simulated and observed spatial patterns. They found that the injection altitude of the BrO plume was located between 8 and 12 km altitude, i.e., in the upper troposphere/lower stratosphere region. Despite the fact that BrO and SO_2 are two different gases, it is likely that the gases are emitted roughly at the same height intervals, this is also proved by good correlation between the spatial extent of the SO_2 plume and the BrO plume measured simultaneously by GOME-2. The identified BrO emission altitude agrees with the peaks at ∼8-9 km and ∼12 km in the inversion profiles of SO_2.

4.3 Consistency check

Figure 4.4 shows the AIRS satellite measurements used in the inversion method, the FLEXPART data used as input to the method (a priori), and the FLEXPART simulation when using emissions according to the inversion profile (a posteriori). This is not a real validation of the estimated profile, rather a consistency check. If the satellite data are reproduced closely, this will confirm that the inversion algorithm is basically working. However, this satellite overpass is not the only one used in the inversion method, the other overpasses that are used also affect the solution, so a total match between the satellite overpass and the a posteriori is not expected. For the FLEXPART figures, the left panel shows the horizontal dispersion while the right panel shows the height distribution when mass is integrated over all latitudes.

To obtain a better comparison with the AIRS satellite measurement, both the FLEXPART data used in the inversion method, and the FLEXPART data obtained when using the a posteriori profile, are weighted with the AIRS infrared weighting function showed in figure 3.5. This is done because the AIRS instrument is not able to measure the low level emissions.

The satellite overpass on 8 August at 13:41 UTC is shown in figure 4.4(a). This is the first of ten overpasses that are used in the inversion method. The emissions have been transported into a "croissant"-shape due to a passing cyclone. Some maxima are located south of the volcano.

The model input to the inversion shown in the figures 4.4(b) and 4.4(c), represent the constant a priori profile. This simulation was obtained with unit mass in each layer, so a scaling with the total a priori mass was performed to be able to compare this simulation with the a posteriori and the satellite measurement. The emissions above 15 km are barely not transported at all and are clearly contributing to the maximum located close to the volcano. The emissions from the height range around 10 km are transported into the "croissant"-shape.

Figure 4.4(d) and 4.4(e) show the model simulation with the AIRS inversion profile as input, the so-called a posteriori. The emissions above 15 km are strongly reduced compared to the a priori, while the lower emissions are increased. There are two maxima southeast of the volcano. By investigating the emissions more closely it is found that these maxima are located in the height range 11-12 km. The maximum located northeast of the volcano is located at about 9 km altitude.

Comparing the a priori and the a posteriori with the satellite measurements there is obviously no high maximum located just above the volcano, so for the a priori profile, the high emissions above 15 km are not found in the measurements. It is the a posteriori profile that reproduces the observed pattern closest, and especially the two maxima southeast of the volcano. However, there are also certain differences. The maximum northeast of the volcano is not found in the measurements. It seems like FLEXPART transports some of the emissions faster than what is observed, also the northeast maximum is stronger than what is observed. This can be explained by a quick look at figure 4.17 in the coming section 4.7.1. This figure shows the inversion profile when using only this overpass (turquoise line), and it can be seen that the 9 km peak is strongly reduced when using only this measurement. This implies that the maximum northeast of the volcano is not consistent with this measurement, thus is not determined by this overpass but is produced to improve agreement with later observations.

Furthermore, this AIRS overpass shows a smaller total amount of mass than at later times. The total mass for the satellite observation is 0.28 Mt. The total mass of both the a priori and the a posteriori is on the order of 1.2 Mt, thus generally higher than what is found by the measurements. However, referring again to figure 4.17, the total a posteriori mass is lower (0.48 Mt) when using only this satellite overpass in the inversion algorithm.

In addition, there might also be discrepancies due to different weighting function used for this AIRS retrieval and the weighting function that is applied on the FLEXPART data.

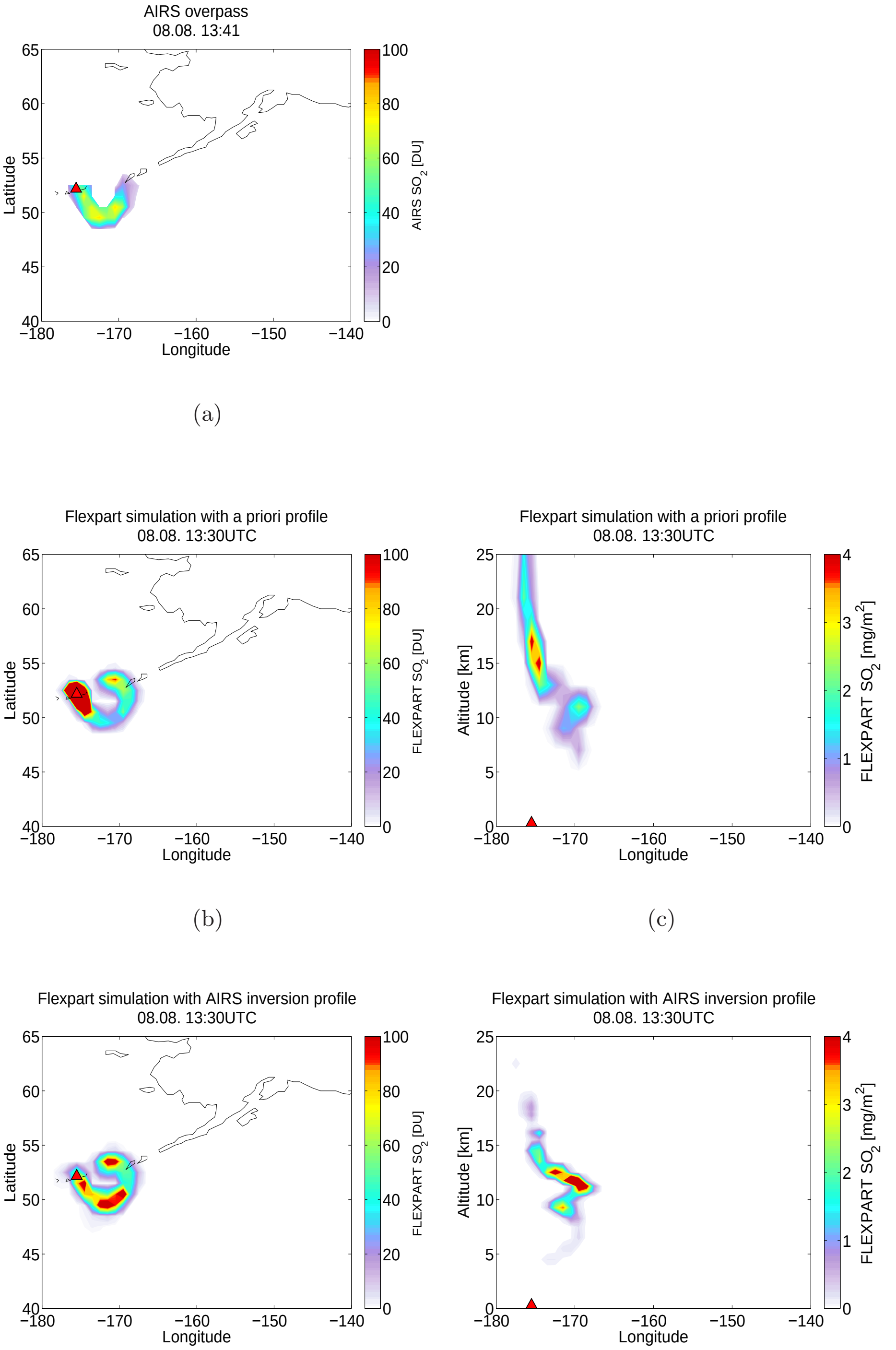

(a)

(b) (c)

(d) (e)

Figure 4.4: *Comparison of one of the satellite overpasses used in the inversion method, the FLEXPART data used as input to the method (a priori), and the FLEXPART simulation using emissions according to the inversion profile (a posteriori) from figure 4.1(b). The left panel shows the horizontal dispersion while the right panel shows vertical zonal plots where mass is integrated over all latitudes. The infrared weighting function of figure 3.5 is applied to both the a priori and a posteriori FLEXPART data.*

Figure 4.5 shows the same type of data as the previous figures. However, no weighting function is applied to the FLEXPART data, thus this is an illustration of how the weighting function affects the results. The weighting function decreases the lower emissions as well as the highest according to the lower sensitivity of the satellite measurements at these heights.

These figures also give an impression of where the lower emissions are transported. The emissions from ground up to about 5 km are transported northwest and later southwards to join the rest of the emissions in a circular shape.

Still, when considering the FLEXPART figures without the use of the weighting functions, the a posteriori, with decreased emissions above 15 km and increased lower emissions, is a closer match to the satellite overpass than the a priori. It seems like the lower emissions are transported rather quickly to join the rest of the plume, thus ground level emissions (where the transport is slowest) are not occurring, as evident from the AIRS inversion profile.

Given that the AIRS satellite is not able to observe these low level emissions it is difficult to determine whether these emissions are real or not by comparing with AIRS satellite measurement. However, the inversion method still finds a combination of some satellite measurements that match these low level emissions. Also, as mentioned in the previous sub chapter, when using OMI data for the inversion, with a greater accuracy for the lowest levels, there is also estimates on low level emissions which are reduced when compared to this AIRS inversion profile.

In summary, the inversion profile yields a better match with the satellite measurement than the a priori profile. The good agreement shows that the ECMWF winds are compatible with the actual dispersion of the volcanic plume and that FLEXPART can handle the transport simulation very well. Because this satellite overpass is not the only one used and because of uncertainties in the lower altitude emissions, some discrepancies between the observations and the a posteriori are found, especially considering the amount of mass. It is believed that the inversion profile will give a good estimate for the transport of the eruption.

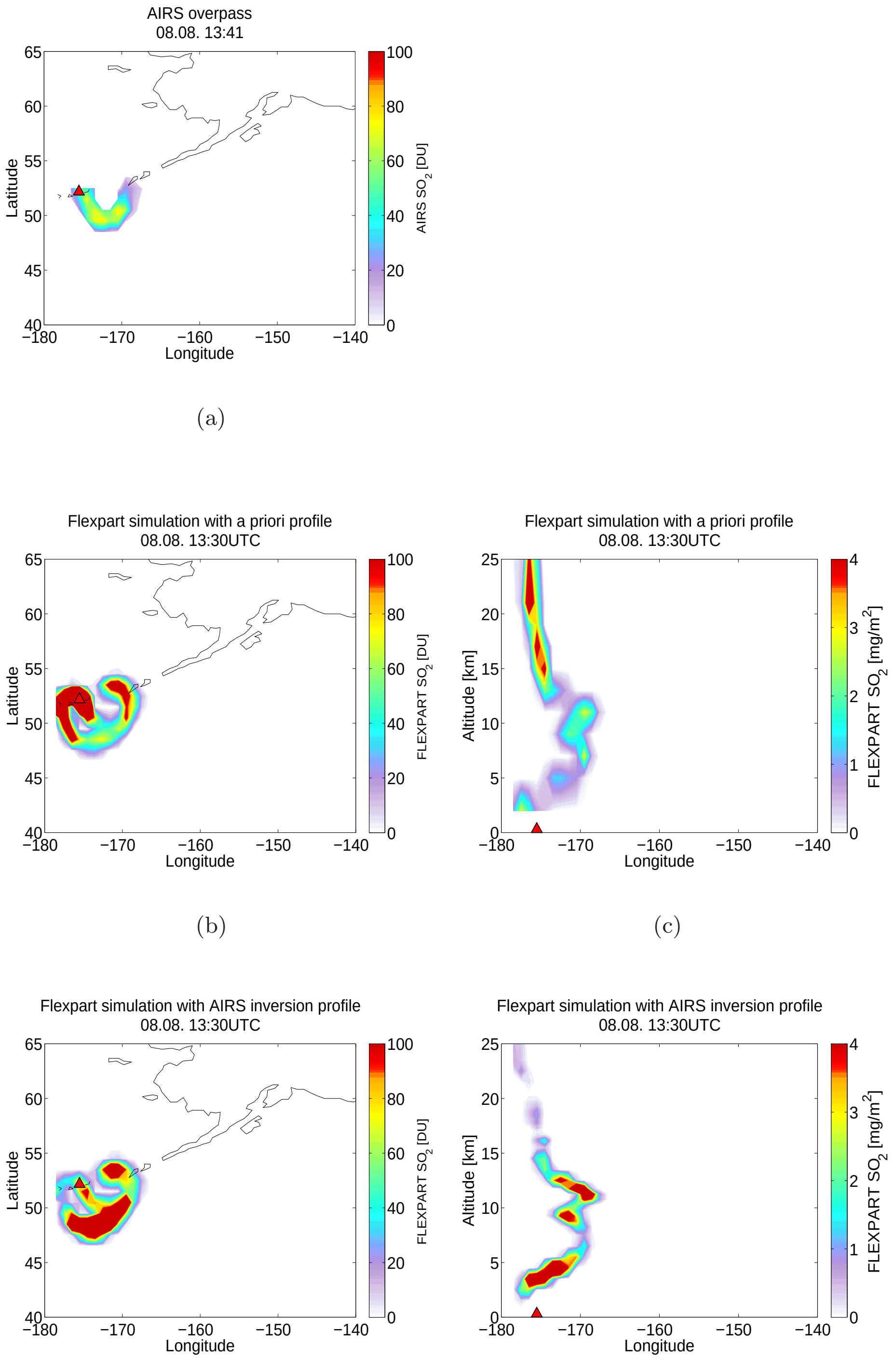

(a)

(b) (c)

(d) (e)

Figure 4.5: *Comparison of one of the satellite overpasses used in the inversion method, the FLEXPART data used as input to the method (a priori), and the FLEXPART simulation using emissions according to the inversion profile (a posteriori) of figure 4.1(b). The left panel shows the horizontal dispersion while the right panel shows vertical zonal plots where mass is integrated over all latitudes. No weighting function is applied on the FLEXPART data.*

4.4 Transport

4.4.1 Atmospheric conditions

The weather station at Adak Island (51.86°N, 176.63° W), close to Kasatochi Island, reported of an average temperature of 9.1°C, and wind in an northeasterly direction on 7 August 2008 (Weather Station History, 2008). Pressure was falling during the course of the day. On 8 August the pressure increased, which suggest a low pressure system was passing the area from 7 to 8 August, as illustrated in figure 2.6 in the background chapter. The ECMWF meteorological data used for simulation with FLEXPART are shown in figure 4.6. The wind profiles at the nearest grid point to the volcano (52° N,178° W) around the eruption onset are shown in figure 4.6(a). Wind profiles from 2° south of the volcano, six hours later, are shown in figure 4.6(b), and wind profiles from 5° east of the volcano about ten hours after the eruption, are presented in figure 4.6(c). The emissions were transported southwestward during the first few hours after the eruption. When reaching the areas south of the volcano the winds shift and the emissions are transported southeastward. Further east the wind shifts to a southerly directions and the emissions are transported northwards. After about 15 hours some of the emissions are again passing over the area of the volcano after they have travelled in a counterclockwise spiral due to the flow in the cyclone passing over the area. The figures also show the tropopause located at about 9.5 km.

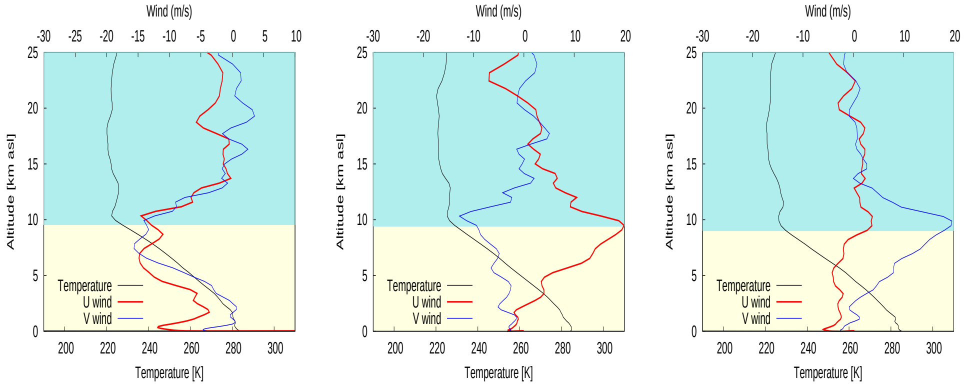

(a) 7 August 21 UTC
Near the volcano

(b) 8 August 03 UTC
2° south of the volcano

(c) 8 August 09 UTC
5° east of the volcano

Figure 4.6: *ECMWF vertical profiles of temperature and wind for specified locations at different hours before and after the eruption onset. The yellow and turquoise background shadings indicate the troposphere and the stratosphere, respectively.*

4.4.2 Transport with inversion profile

The simulation of the transport of the volcanic SO_2 plume using the inversion profile of figure 4.1(b) as emission height profile, is illustrated in the figures 4.7 and 4.8. The left panels show the horizontal dispersion of the SO_2 plume as well as the 200hPa geopotential height given in decametres, which are taken from the ECMWF analysis at 18:00 UTC. The 200hPa geopotential height is the most relevant altitude for the long-range transport. The right panels show vertical zonal plots where mass is integrated over all latitudes. The position of the volcano is marked with a red triangle, $\triangle$. Also shown are the LIDAR positions of the LIDARs at Nova Scotia (green dot) and Ny Ålesund (blue dot).

Figure 4.7(a) and 4.7(b) show the plume 20 hours after the eruption. The plume has mainly drifted southeastward from the volcano over the Pacific Ocean where it has spread out in a characteristic circular shape due to the flow in the passing cyclone. It is the emissions around 8-9 km that is transported fastest into this circular shape, and it is seen from the height plot that the emissions around 9 km are at this time again located in the area above the volcano. It is also possible to identify the inversion profile of figure 4.1(b), with mass peaks at $\sim$5 km, $\sim$9 km and $\sim$12 km.

The further transport of the plume is shown on the following figures. On 10 August, 3 days after the eruption, one part of the plume at an altitude around 12 km is separated and travels eastward faster than the rest of the plume. This part of the SO_2 cloud hits the coast of Alaska at Prince of Wales Island (55.6° N, 132.9° W). ECMWF wind profiles for this location at this point of time (not shown), indicate strong westerly winds in the altitude range 5-15 km where the plume is located.

Hitting the coast the plume splits into two, as seen in figure 4.8(a). One part of the plume is transported across the northern part of Canada towards Greenland. The other part spreads towards Chicago across the Northern U.S. After 5-6 days the plume reaches the Atlantic Ocean, as illustrated by the last figures. Furthermore, Europe was hit by the plume within a week after the eruption.

It is clearly the efficient transport near the tropopause by the jet stream that results in the fast transport of the plume across North-America. However, the main part of the plume is found over Alaska during the days following the eruption.

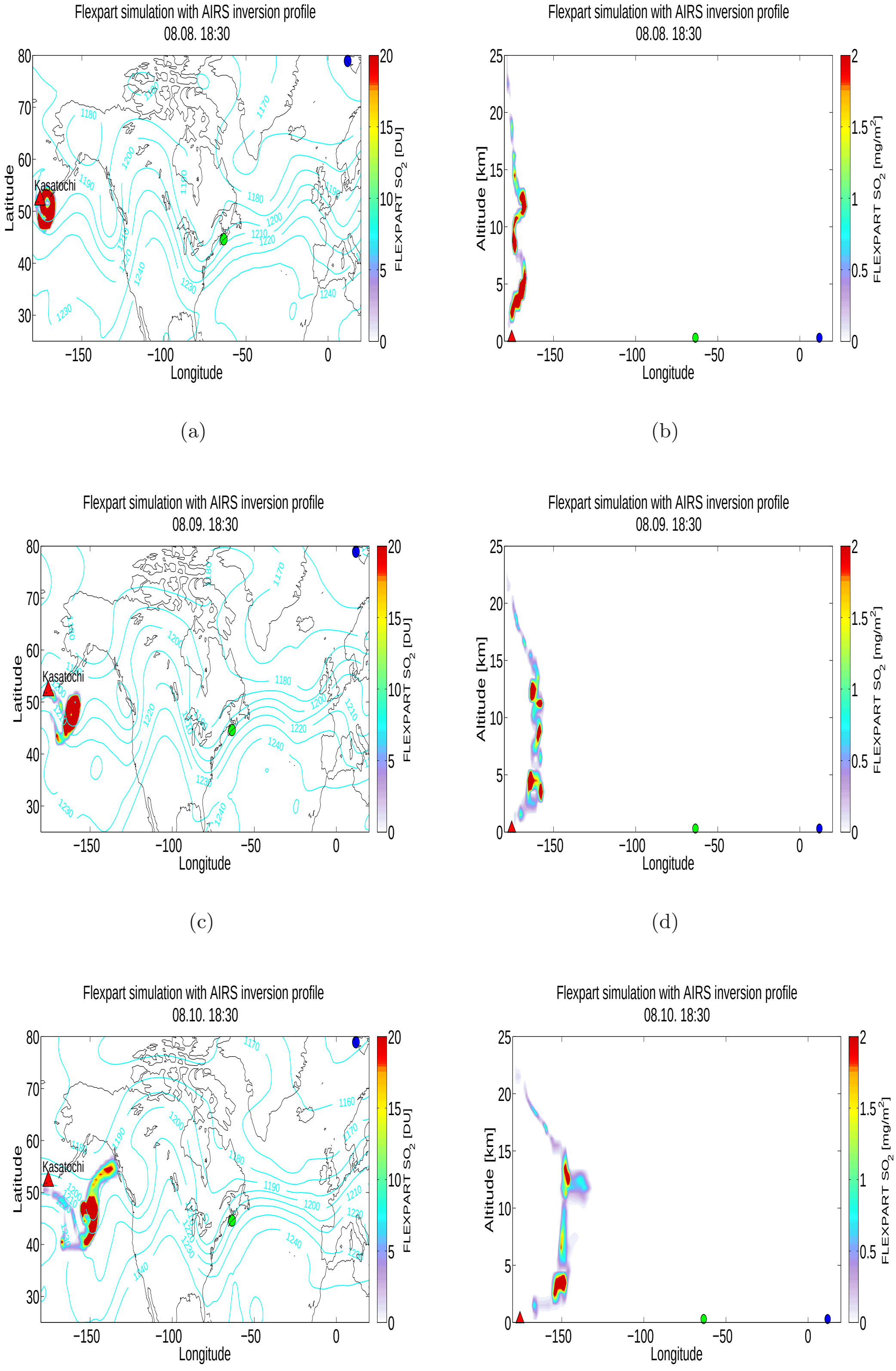

(a) (b)

(c) (d)

(e) (f)

Figure 4.7: *General transport of the SO_2 plume from Kasatochi, 8-10 August, simulated by FLEXPART using the emission profile from figure 4.1(b). The left panel shows the horizontal dispersion and 200hPa geopotential height [dkm]. The right panel shows vertical zonal plots where mass is integrated over all latitudes.*

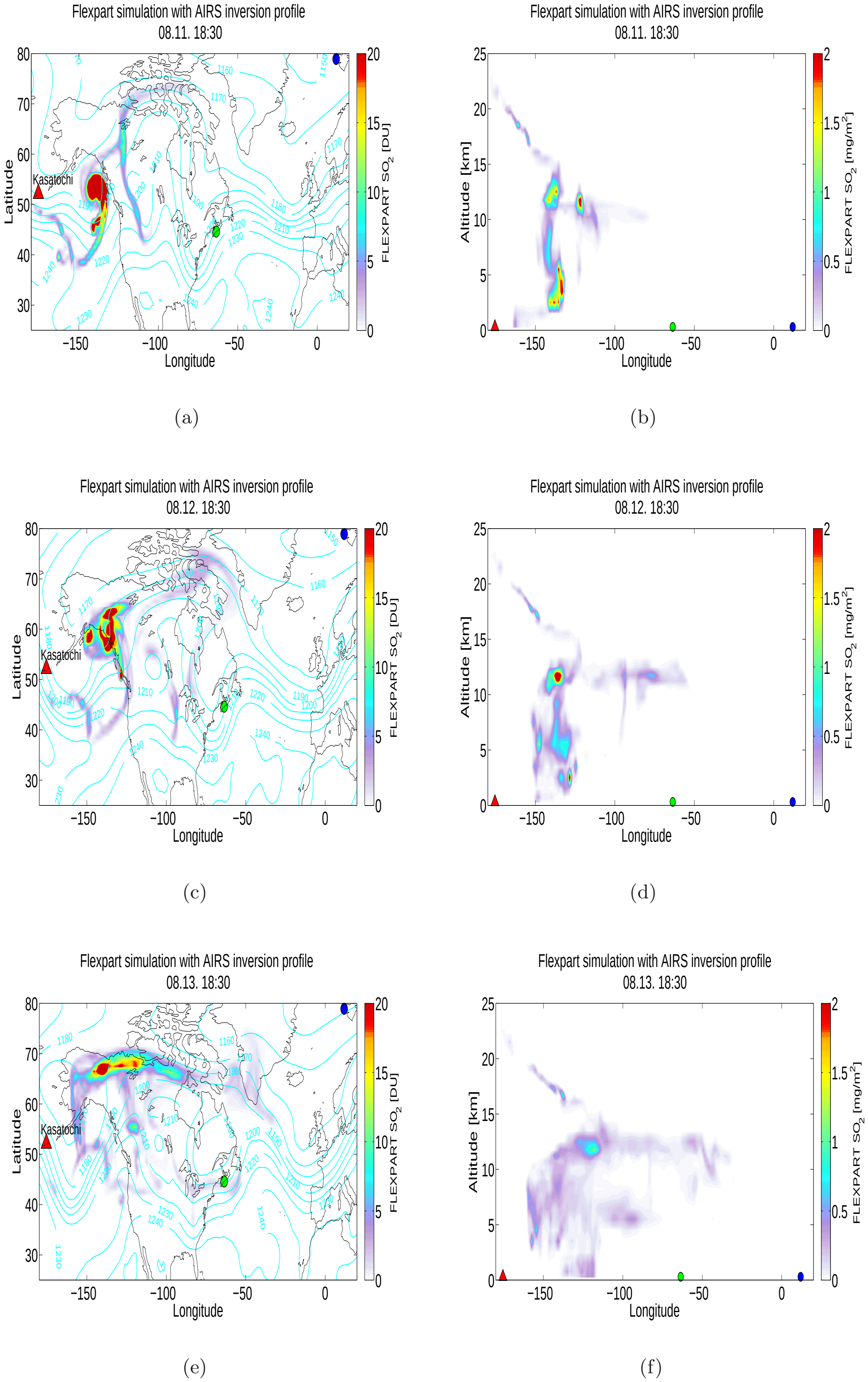

(a) (b)

(c) (d)

(e) (f)

Figure 4.8: *General transport of the SO_2 plume from Kasatochi, 11-13 August, simulated by FLEXPART using the emission profile from figure 4.1(b). The left panel shows the horizontal dispersion and 200hPa geopotential height [dkm]. The right panel shows vertical zonal plots where mass is integrated over all latitudes.*

4.5 Comparison with uniform height profile

An important consideration is how the long-range transport of the emissions according to the inversion profile compares to transport with a uniform height emission profile, as is currently used by the VAACs without available information on the height profile. A uniform distribution represents the constant a priori of the inversion.

Figures 4.9 and 4.10 compares the horizontal and vertical transport patterns of the two different height emission profiles. The upper panel shows the transport using the uniform profile, while the lower panel shows the transport using emissions according to the estimated emission height profile. The spatial patterns can look quite similar but the mass at each point is clearly different. These is more mass in the high altitudes using a uniform profile. By comparing figure 4.9 with the AIRS satellite measurement around 11 hours earlier on 9 August at 23:53 UTC that is shown in figure 3.2(a) (section 3.2.1), there are no observations of a distinct "tail" of the plume as the uniform emission profile show. Thus the flexpart simulation using the inversion profile gives the closest match to the satellite observation (the general discrepancies between the satellite measurements and the model simulation is due to not using a weighting function on the FLEXPART data.)

For the uniform height profile an assumption has to be made about the top altitude of the emissions. The current uniform height profile has top emission height at 20 km. It is mainly the emissions from the height levels between 15-20 km that are not in agreement with the transport using the inversion profile. The mass at these altitudes is too high compared to the inversion transport. By constraining the uniform emission height profile with a top emission altitude at 15 km the patterns and mass at each point would be more similar. However, the inversion profile shows smaller emissions above 15 km, which are of special climatic importance. Thus, a uniform height profile can give inaccurate results if the height emission profile is to be used for a climatic application.

Furthermore, a volcanic eruption can in general emit mass up to 30 km or more. The spatial transport pattern of a uniform profile with a top at 30 km would certainly differ even more from the patterns of the inversion profile. Still, given information on the cloud top height, a uniform height profile would not be an overall bad assumption if only considering the spatial distribution and not the amount of mass at each location, or the amount of SO_2 reaching deep into the stratosphere. However, the amount of mass at each height level below 10 km is especially important for aviation purposes so that it is possible to avoid regions that exceed certain risk limits for the concentration level.

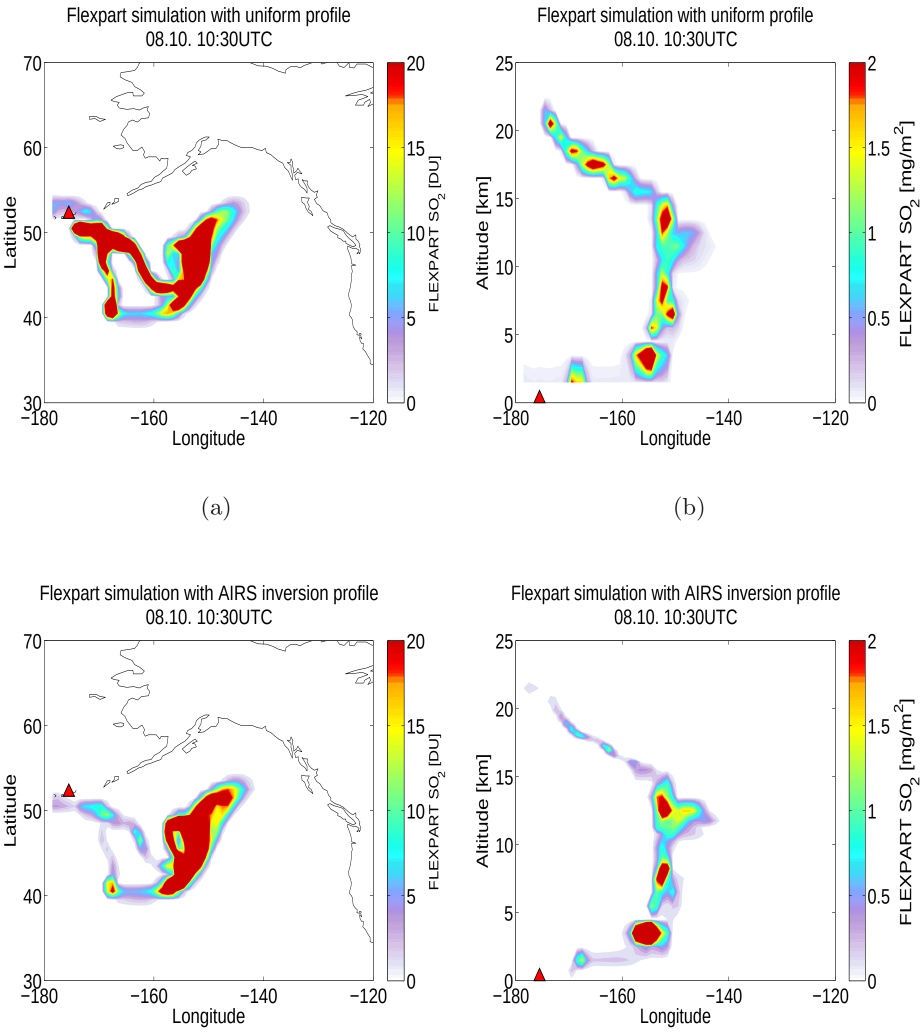

(a) (b)

(c) (d)

Figure 4.9: *Transport of* SO_2 *emissions from Kasatochi, simulated by FLEXPART for 10 August at 10:30 UTC. The top panel shows the model simulation using a uniform height emission profile and the lower panel shows the model simulation using emissions according to the inversion profile from figure 4.1(b). The figures on the left panel show the horizontal dispersion while the figures on the right panel show vertical zonal plots where mass is integrated over all latitudes.*

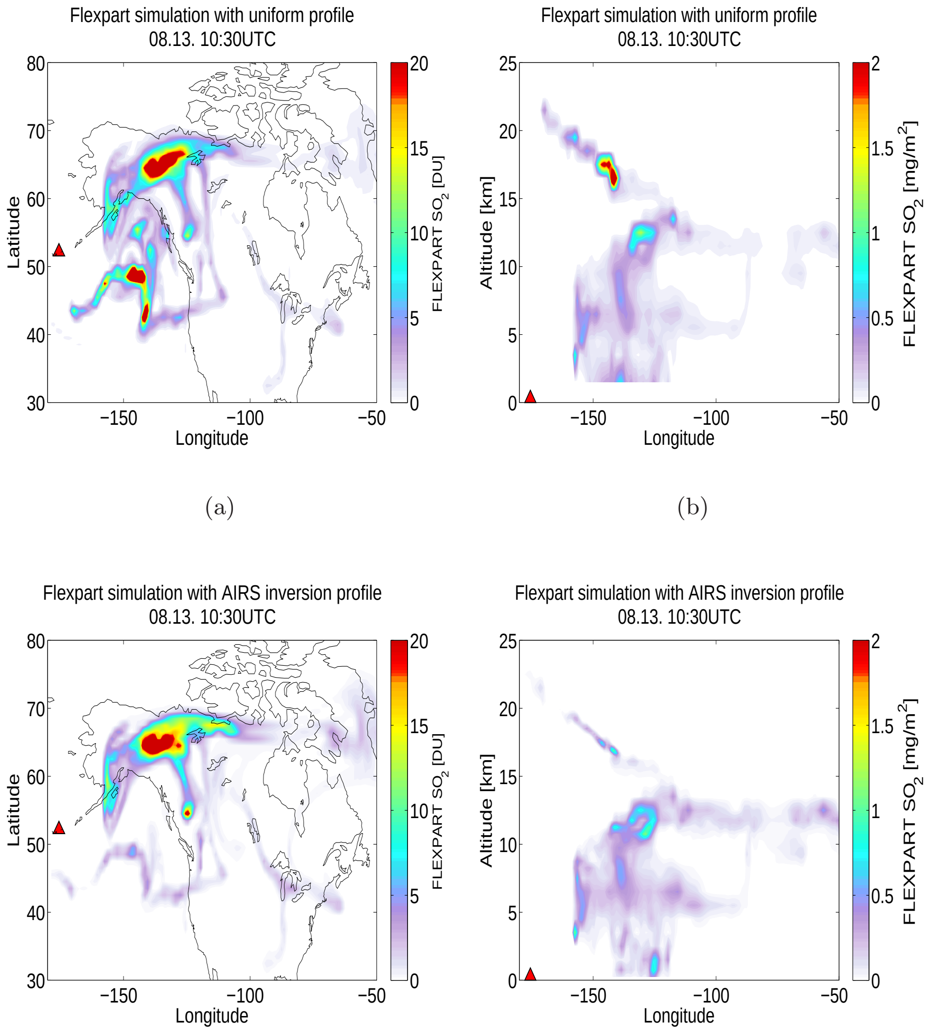

(a) (b)

(c) (d)

Figure 4.10: *Transport of SO_2 emissions from Kasatochi, simulated by FLEXPART for 13 August at 10:30 UTC. The top panel shows the model simulation using a uniform height emission profile and the lower panel shows the model simulation using emissions according to the inversion profile from figure 4.1(b). The figures on the left panel show the horizontal dispersion while the figures on the right panel show vertical zonal plots where mass is integrated over all latitudes.*

4.6 Validation of the inversion profile

The estimated emission height profile is validated by comparing a FLEXPART simulation using the default emission profile from figure 4.1(b) as input, with independent observations of the volcanic plume, such as AIRS and OMI data which are not used for the inversion. Also LIDAR measurements are used to evaluate the height of the simulated plume.

4.6.1 Comparison with independent satellite data

First, the FLEXPART simulation using the emission profile from figure 4.1(b) as input is compared with independent AIRS data, that is, measurements which are not used in the inversion method. Figure 4.11 shows the model simulation for 11 August at 21:30 UTC, 4 days after the eruption, and an AIRS observation about half hour later, at 22:05 UTC. The SO_2 plume is observed over the coast of Alaska close to the Canadian border. The AIRS observation does not show the "end-tail" of the plume over the Pacific ocean, nor the "front-tail" east of 125° W, this is due to insufficient swath width of the overpass. The swath width boundaries are marked with grey lines. The FLEXPART column values showed in the left figure are weighted with the AIRS infrared weighting function from figure 3.5.

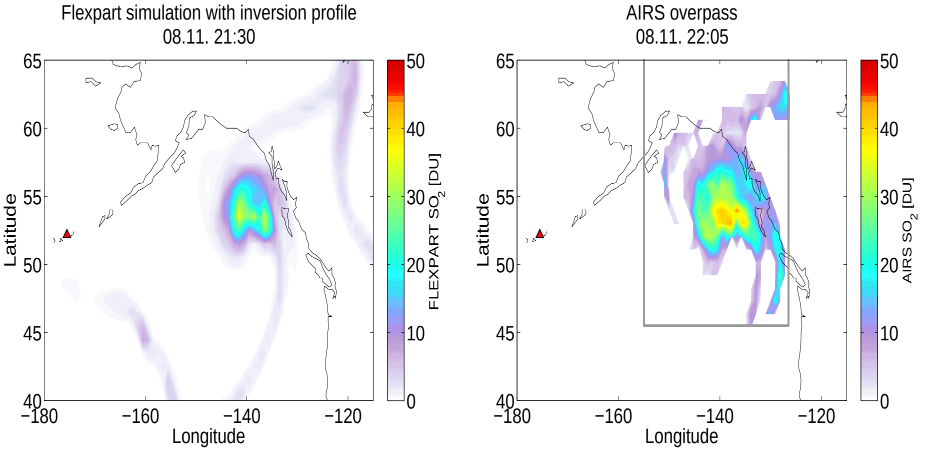

(a)

(b)

Figure 4.11: *a) SO_2 columns for 11 August at 21:30 UTC, simulated by FLEXPART using emissions according to the inversion profile showed in figure 4.1(b). The IR weighting function from figure 3.5 is applied to the FLEXPART data. b) SO_2 columns measured by the AIRS satellite instrument on 11 August at 22:05 UTC. The swath width boundaries of the overpass are marked with grey lines.*

For areas covered by the AIRS observation there is very good agreement between the model simulation and measurement data. Especially, the shape of the plume is simulated very well with a distinct sharp bend of the plume at the southern end. However, the maximum SO_2 measurement value close to 50 DU in center of the plume, is too low in the FLEXPART simulation, thus the model underestimates the amount of SO_2. This is possibly due to the SO_2 loss by dry deposition and by reaction with OH which is only estimated by FLEXPART and is quite uncertain. Furthermore, the IR-kernel applied to the FLEXPART column values, can be different from the IR-kernel used for this AIRS observation, and can lead to differences in the amount of SO_2.

Secondly, the FLEXPART simulation using the estimated emission height profile is compared with independent OMI data, as well as GOME-2 satellite measurements. GOME-2, similar to OMI, measures backscattered solar radiation in the ultraviolet spectrum. On 12 August at 21:30 UTC, five days after the eruption, the main part of the SO_2 plume has travelled northeast and is located around Wrangell St. Elias national park in Alaska. The front tail of the plume has reached Greenland, as seen in figure 4.12(a) which shows the FLEXPART simulation for this day. The FLEXPART data have been weighted with the UV weighting function showed in figure 3.5. Figure 4.12(b) and 4.12(c) show on the current day the OMI and GOME-2 satellite observations, respectively. For comparison with FLEXPART it is important to consider the different time scales of the figures. While the model results show a snapshot of the dispersed SO_2, the satellite observations are composites of data collected for various moments during the day.

Comparing the FLEXPART simulation with the OMI satellite observations, there is an overall good agreement and the transport of the plume is simulated very well. Nevertheless, there are some discrepancies regarding the mass. It seems like for the FLEXPART simulation there is more mass in the main part of the plume, while there is less mass in the tails compared to the OMI observations. Using the OMI inversion profile from figure 4.2(b) for the transport simulation will possibly result in more mass in the front tails as the ∼12 km peak is increased compared to the AIRS inversion, and the front tails originate and are found near 12 km (see the transport figures 4.7 and 4.8).

Comparing to the GOME-2 measurements there are also very similar transport patterns, but GOME-2 shows even more mass both in the front and end tails for the plume. The general discrepancies regarding mass are possibly due to the estimated loss rates of SO_2 and also the different weighting functions applied to the FLEXPART data and the weighting functions used for the satellite retrievals. By comparing the OMI observations with the GOME-2 observations it seems like there are some OMI overpasses missing. Between 130°E-145°E, both the GOME-2 satellite measurements and the FLEXPART simulation show a tail at 40°N as well at more SO_2 on the western side of the main part of the plume. In addition, the front part of the plume reaching Greenland is not visible in the OMI figure. Also some supposed artificial observations by OMI (possibly due to errors in the retrievals) on the northern part of Alaska are visible.

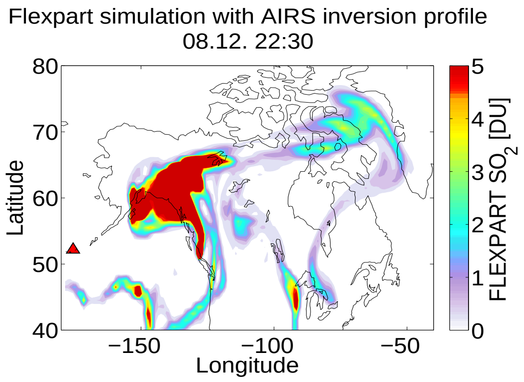

(a) FLEXPART

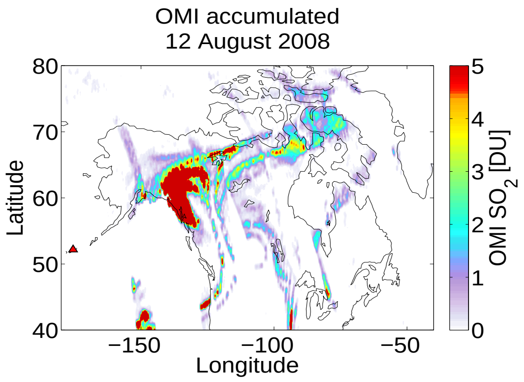

(b) OMI

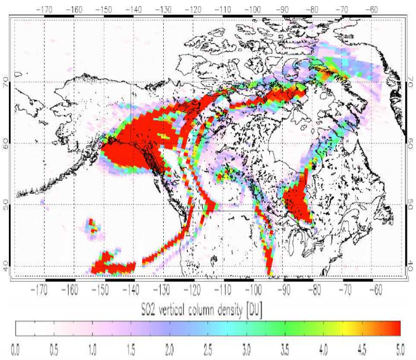

(c) GOME

Figure 4.12: *a) SO_2 columns for 12 August at 22:30 UTC, simulated by FLEXPART using the emission profile from the inversion showed in figure 4.1(b). The UV weighting function from figure 3.5 is applied to the FLEXPART data. b) SO_2 columns measured by OMI and c) GOME-2 (from: Rix et al. (2008)), both accumulated for 12 August.*

4.6.2 LIDAR measurements, Nova Scotia

The Kasatochi plume was observed by the LIDAR at Nova Scotia (44.6° N, 63.6° W) on the eastern coast of Canada. The position of the LIDAR is marked by a green circle in center of the transport figures 4.7 and 4.8. These transport figures suggest that the plume first reached Nova Scotia on 13 August at an altitude of about 12 km. However, the measurements of the plume were available from 21 August and the days following, at an altitude around 18 km.

Figures of the LIDAR measurements were prepared by Lubna Bitar at Dalhousie University. A FLEXPART simulation, with the inversion profile from figure 4.1(b) as input and a vertical output resolution of 200 m, was plotted in the same manner as the LIDAR observations. The LIDAR figures are shown in the upper panel in figure 4.13 and in figure 4.14, where figures on the left handside are the real LIDAR measurements, and the FLEXPART LIDAR plots are shown to the right.

It is important to keep in mind that only qualitative comparisons of these plots are possible. This is explained in the previous section 3.4, and is due to the fact that the LIDAR observes aerosols rather than sulphur dioxide gas. The plots are used for evaluation of the altitude of the simulated plumes.

The upper panel in figure 4.13 show the measurement and simulation on 21 August. There is convincingly good agreement between the observed layer at 18 km, and the FLEXPART simulation of the plume. However, the simulated plume is located slightly higher than the observed layer.

The scientists at Dalhousie University made backward trajectory calculations with the HYSPLIT model based on the observations, shown in figure 4.13(c). The source of the observed layer is identified to the area of the Kasatochi Volcano and the emission height of this observed layer is estimated to about 17.5 km by the backward trajectory calculations. The emission source of the observed layer is investigated further by using FLEXPART to simulate the transport of only the $\sim$18 km emission peak of the inversion profile in figure 4.1(b). This is illustrated in figure 4.13(d) which is an accumulated plot over the days 7-21 August. The emissions at $\sim$18 km are dispersed to the area of the LIDAR (green circle) by 21 August. Doing the same with the emission peak at $\sim$12 km showed no 18 km layer over Nova Scotia on 21 August (not shown in the figure). So, it is most likely the emissions originating from $\sim$18 km that is observed by the LIDAR, thus the LIDAR measurement provide validation of this part of the inversion profile.

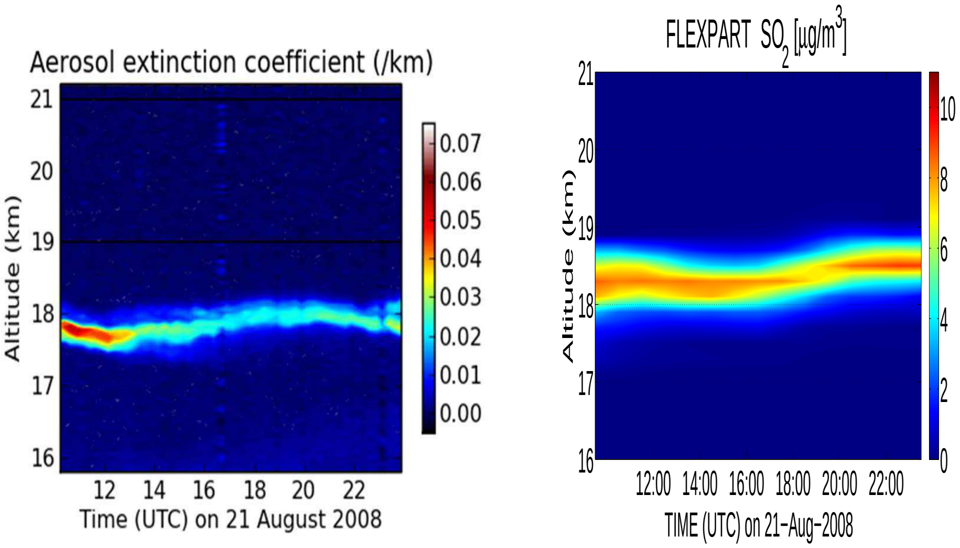

(a) LIDAR (b) FLEXPART

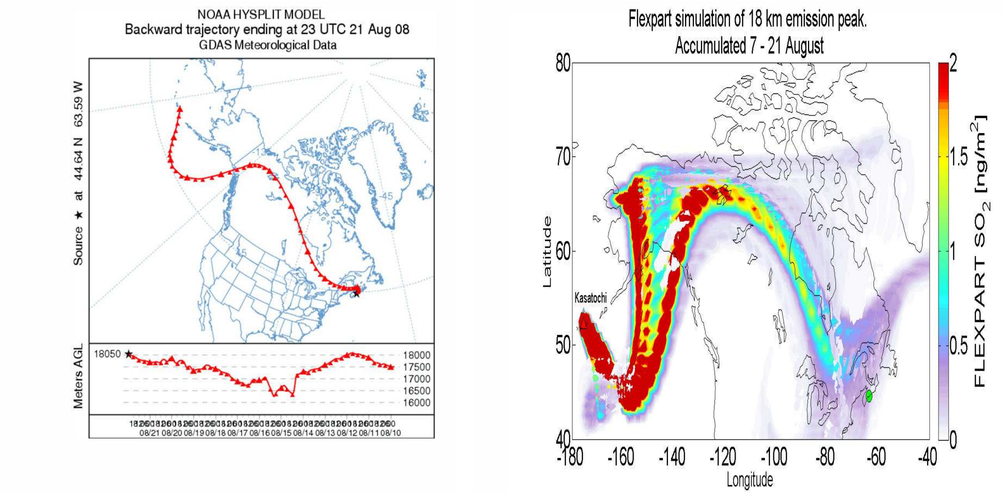

(c) HYSPLIT (d) FLEXPART

Figure 4.13: *Upper panel shows the LIDAR measurements (left figure) from Nova Scotia on 21 August and SO_2 levels simulated by FLEXPART (right figure) for the location of the LIDAR, on the same day. Emissions according to the inversion profile from figure 4.1(b) is used for the model simulation. The lower panel shows a HYSPLIT backward trajectory calculation (left figure) and an accumulated plot of SO_2 columns from a FLEXPART simulation using emissions at 18 km altitude only (right figure).*

The following day, on 22 August, the simulated plume is still in agreement with the observed layer at 18 km, as seen in the upper panel in figure 4.14. Moreover, it was believed to be tropospheric detection of the volcanic plume as well. However, this tropospheric observed layer around 12 km is probably only observations of clouds since it is not present in the model simulation.

On 8 September, over one month after the eruption of Kasatochi, there are still observations of a stratospheric layer around 18 km, illustrated in figure 4.14 (lower panel). The FLEXPART simulation shows very weak layers located higher than the observations. Notice the different scale of this plot. Despite the fact that the altitude of the layers do not agree very well, it is evident that there still are debris of the Kasatochi plume visible over Nova Scotia.

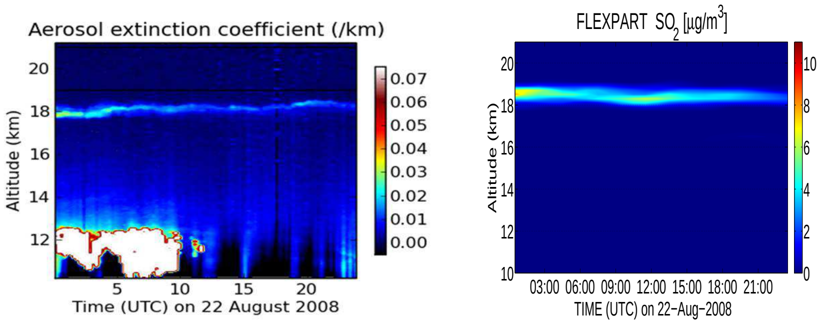

(a) LIDAR (b) FLEXPART

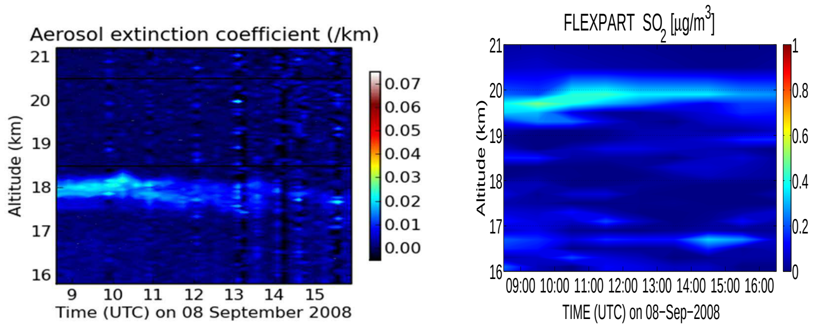

(c) LIDAR (d) FLEXPART

Figure 4.14: *LIDAR measurements (left panel) from Nova Scotia on 22 August and 8 September.* SO_2 *levels simulated by FLEXPART (right panel) for the location of the LIDAR on the same days. Emissions according to the inversion profile from figure 4.1(b) is used for the model simulation.*

4.6.3 LIDAR measurements, Ny Ålesund

The Kasatochi plume was also observed by the LIDAR at Koldewey Station (78.9° N, 11.9° E), Ny Ålesund, Svalbard. The position of the LIDAR is marked by a blue circle in the top right corner in the transport figures 4.7 and 4.8.

LIDAR measurements were made available from AWI and table 4.1 gives a survey of the observations. The observations were taken from 15 August to 5 September 2008.

DATE / TIME (UTC)	**OBSERVED LAYER**
15.08.08 / 8 and 10-12	11-12 km
25.08.08 / 12:30	11-12 km and 14 km
29.08.08 / 08-08:30 and 09-12:30	10-12 km and 15 km
31.08.08 / 20:00	10-12 km
01.09.08 / 12-13 and 14-24	10-12 km and 17 km
03.09.08 / 09:30	9-11 km (clouds 7-8 km)
05.09.08 / 7-8	9-11 km and 16 km.
05.09.08 / 19-20	9-10 km and 13 km.

Table 4.1: *LIDAR observations at Koldewey Station, Svalbard.*

A FLEXPART simulation, using emissions according to the inversion profile from figure 4.1(b) and a vertical resolution of 200 m was plotted in the same manner as the LIDAR observations. Two figures representing the observations were available. These are shown to the left in figure 4.15 and compared with the FLEXPART simulation shown to the right.

On 15 August, 8 days after the eruption, the Kasatochi plume was thought to be observed in a layer within 11-12 km height range, but this is not seen in the FLEXPART simulation. However, a layer around ∼9 km is seen in the model simulation, and the LIDAR observation also indicate a layer at this height. By exploring the emission source of this layer it was found that this layer originate from emissions around 9-10 km.

On 3 September, 27 days after the eruption, LIDAR observations around 09:30 UTC show clouds from 7-8 km, and an aerosol layer from 9 to 11 km. This is shown in figure 4.15(c) (blue line). From the FLEXPART simulation the layer at this altitude is visible, furthermore, a layer around 17 km is also present. This layer is also found in the LIDAR observation.

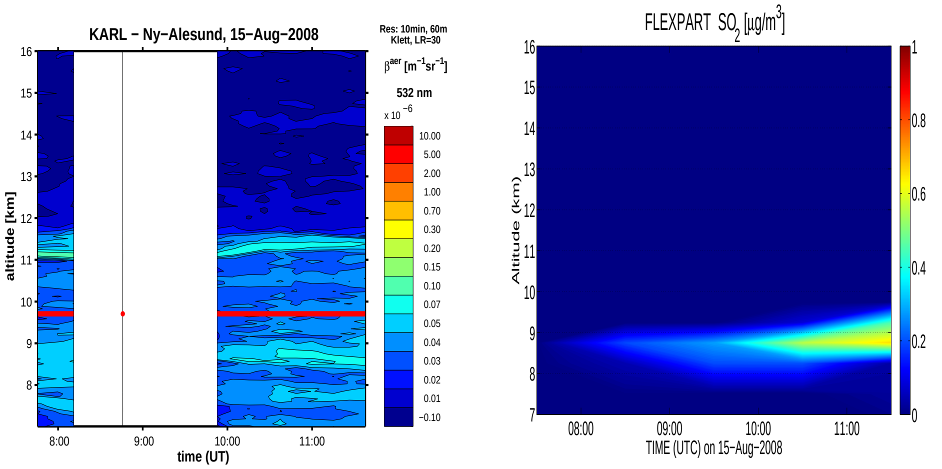

(a) LIDAR, 15 August

(b) FLEXPART, 15 August

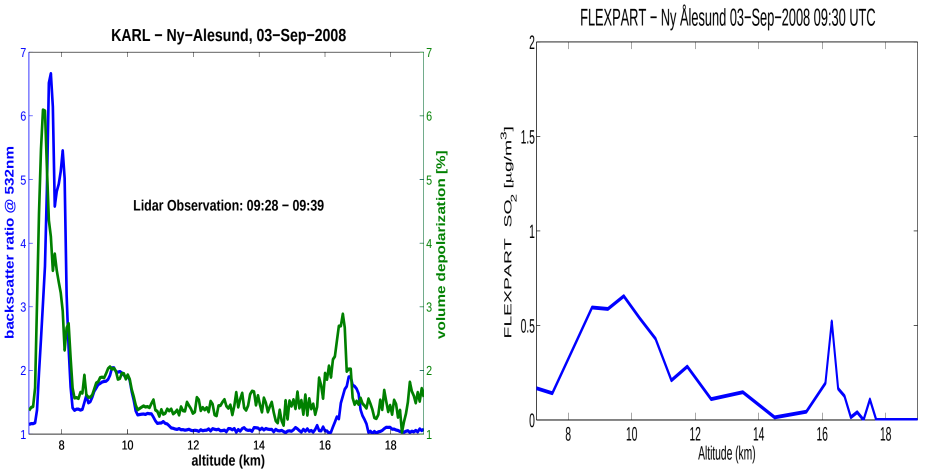

(c) LIDAR, 3 September

(d) FLEXPART, 3 September

Figure 4.15: *LIDAR measurements (left panel) from Ny Ålesund on 15 August and 3 September, compared with* SO_2 *levels simulated by FLEXPART (right panel) for the location of the LIDAR. Emissions according to the inversion profile from figure 4.1(b) is used for the model simulation.*

Several other observations were made at the station. Most of these at heights around 11 km, and some observations around 14-16 km. The lower height layers were found in the model simulation, an example shown in figure 4.16 for 31 August. However, the layers observed around 14-16 km could not be identified by FLEXPART and are possibly not related to the eruption of Kasatochi. These layers can originate from a different volcanic eruption, potentially Okmok Volcano close to Kasatochi which erupted a few weeks earlier.

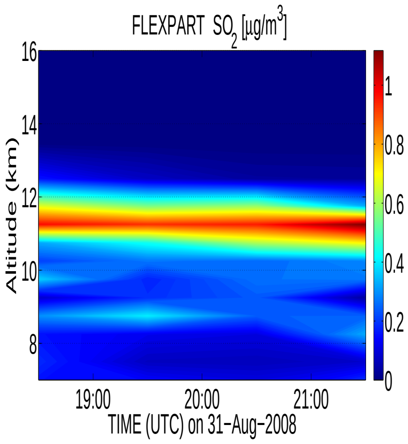

Figure 4.16: *FLEXPART simulation of SO_2 at the location of the LIDAR in Ny Ålesund, 24 days after the eruption of Kasatochi. Emissions according to the inversion profile showed in figure 4.1(b) is used for the model simulation.*

Considering the fact that some of these measurements have been made nearly a month after the eruption of Kasatochi, the comparisons with the FLEXPART simulation are convincingly good.

4.7 Sensitivity studies

Determining the accuracy of the inversion method involves identifying how the inversion results are affected by changes in some of the input parameters to the method. In this study the focus has been identifying how sensitive the inversion profile is to changes in the amount of satellite data used in the inversion method. Also, the sensitivity of the inversion profile on the weighting function (kernel) used for the FLEXPART data which goes into the inversion method, is explored.

4.7.1 Amount of satellite data

It is critical to know the number of satellite observations needed to obtain a meaningful a posteriori emission profile. The errors in satellite retrievals relative to the decreasing SO_2 values in the plume, as well as errors in the model simulation, grow in time. To minimise the impact of these errors, and to make the inversion realistic for near real-time applications, satellite data from the first day after the eruption, or even less, would ideally be used. However, no observations from geostationary satellites were available, and because AIRS overpass only twice per day, it was thought that using satellite data for up to three days after the eruption was needed, and this was used for the default inversion profile showed in figure 4.1.

To explore the sensitivity of the inversion on the amount of satellite data used, different inversions were preformed using different amounts of observations ranging from one to three days after the eruption. The results are shown in figure 4.17. The default inversion profile (red line) is obtained by using satellite data for three days after the eruption (same as in figure 4.1, repeated for comparison).

Using AIRS satellite data for 25 hours after the eruption (blue line), which includes only two satellite overpasses, gives an inversion profile close to the default profile, but the peak around 10-11 km is not found. Including observations from two days after the eruption (green line), with a total of eight overpasses, increase the emissions around 5 km, and the 9 km peak is slightly reduced. Using only one AIRS satellite overpass on 8 August at 13:30 UTC, 15 hours after the eruption, gives a relatively good result for the height emission profile (turquoise line). The peaks can clearly be identified, except for the $\sim$9 km peak, however the estimated mass is lower than when using more data. The difference between using only this overpass and using observations from 25 hours after the eruption is including only one more overpass at about 23:30 UTC on 8 August. These observations show a SO_2 maximum east of the volcano, but the swath width of the overpass was not sufficient to observe the whole cloud. This can be a problem if the overpass cuts off a part of the cloud located at a different altitude. In addition, the observed SO_2 mass of this overpass is higher than the observations at 13:30 UTC, thus increases the 5 km emissions and gives emissions at 9 km.

Using only one OMI satellite overpass on 8 August at 23:30 UTC (yellow line), 25 hours after the eruption, results in two peaks around 6 and 8 km, with the latter peak not found by the AIRS data. The 9 km peak can clearly be identified, and the 12 km peak is increased compared to the default AIRS profile. However, no peak is found around 10-11km.

In summary it seems that satellite data from one or two days after the eruption rather than using data for three days, would have sufficed to give relatively good results for the height emission profile. Using only one satellite overpass gives a relatively good estimate for the profile above 10 km, but the emissions below this altitude are reduced.

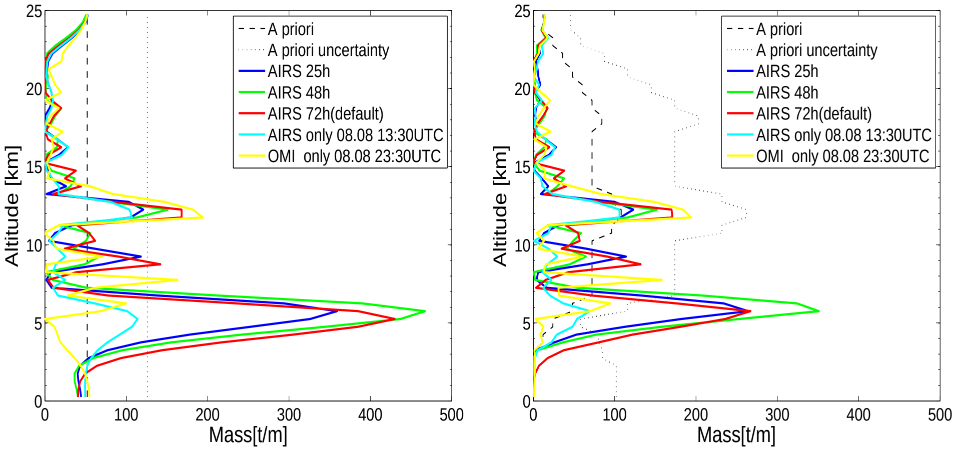

(a) Constant a priori (b) Non constant a priori

Figure 4.17: *Inversion results when using AIRS data from 25 to 72 hours after the eruption, using only one AIRS satellite overpass on 8 August at 13:30 UTC, and when using only one OMI satellite overpass on 8 August at 23:30 UTC. The thick coloured lines show the different inversion profiles of* SO_2 *in tons/meter. The thin dashed line is the a priori profile, the thin dotted line its assumed uncertainty.*

4.7.2 Weighting function

The effect of the weighting function on the inversion profile is explored by applying different weighting functions to the FLEXPART data which go into the inversion. Only inversions using AIRS data were tested. The different inversion results are shown in figure 4.18 together with the respective weighting functions. The default kernel (red line) is the same as in figure 3.5. Also an inversion without use of kernel (blue line) was tested. A normalized kernel (green line) was used, that is a kernel with mean value of 1 so that the total mass is preserved. The analytic kernel (purple line) given in equation 3.5 was used with the height of the absorber peak (z_0) at 12 km, total column abundance $u_0 = 0.1$, inversion parameter $u_1 = 10.0$ and absorption coefficient $k = 0.01$. This function was also changed to allow for an exponential-like function (turquoise line) of the lower height levels.

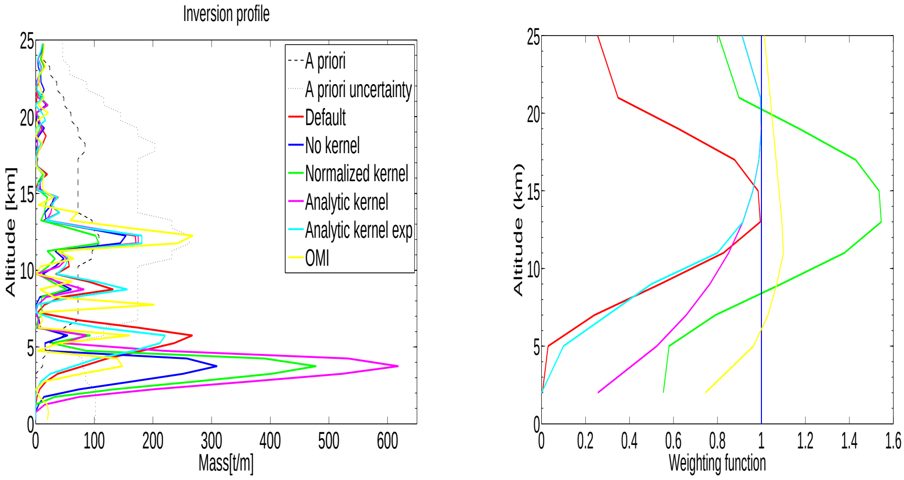

(a) (b)

Figure 4.18: *a) Inversion results when using different kernels (weighting functions) for the FLEXPART data used in the inversion method. The thick coloured lines show the inversion profiles of* SO_2 *in tons/meter. The thin dashed line is the a priori profile, the thin dotted line its assumed uncertainty. b) The corresponding weighting functions.*

The figure shows that the weighting functions have a significant influence on the inversion profile below 10 km. As elaborated in section 3.2.3, AIRS retrievals are restricted to UTLS and thus the default weighting function indicates that the low level SO_2 is observed poorly by the satellite.

The default kernel and the exponential-like analytic kernel show quite similar results as these weighting functions are very similar for the heights below 10 km. Large differences are found when using the normalized kernel, the analytic kernel and without using a kernel. Changing the weighting function for the lowest layer changes the magnitude of lowest emission peak. Also the total mass emitted is changed, as seen in table 4.2.

Inversion profile	**Mass [Mt]**
A priori	1.30
Default	1.18
No kernel	1.02
Normalized kernel	1.29
Analytic kernel	1.83
Analytic kernel exp	1.08
OMI	1.03

Table 4.2: *Total mass in megaton for each inversion profile in figure 4.18.*

Consider changing the weighting function in this specific order: going from no kernel (blue line) to the normalized kernel (green line) and further on to the analytic kernel (purple line). This means the weighting function for the lowest layers decrease from 1 to about 0.25. By doing so the emission peak around 3 km is increased. Thus by decreasing the sensitivity the emission peak increases. This results in an increase of the total mass by 80%, from about 1 Mt to about 1.8 Mt. The inversion method clearly finds a combination of these low level emissions that allow fitting an observation. However, when the FLEXPART sensitivities are weighted with values close to zero, meaning that the sensitivity of the modelled values are very low (i.e., very small value of the source-receptor relationship), the inversion algorithm will try to compensate for this by emitting more mass at this altitude in order to fit the observation.

When the sensitivity is further decreased, as for the default kernel and the analytic exponential kernel, the peak would be increased by an order of magnitude. But this is too costly in terms of deviation from a priori, so the Tikhonov regularization becomes operative and the inversion seeks other solution by constraining the solution more to the a priori.

It is possible to get everything from high to low emissions at low altitudes, depending on how sensitive the satellite data are. The sensitivity at low altitudes is probably quite uncertain and may also be different for different pixels, therefore the low-altitude emissions are very uncertain and can possibly not be trusted in this case.

Investigating the UV retrievals (OMI), which have a different weighting function as shown in figure 3.5, can provide a better constraint for the low level emissions as these retrievals are not constrained to the UTLS. This is clearly the case when considering the OMI inversion result (yellow line, repeated from figure 4.2 for convenience) which shows a highly reduced peak at 5 km, and increased peaks at higher altitudes.

The weighting functions are clearly an uncertain parameter of the inversion method. The weighting functions used in this study is based on a rough estimate of the SO_2 height. The use of individual weighting functions for each gridcell in the domain would provide better results for the inversion profile. As the weighting functions for AIRS depend mostly of the water vapour content as well as the temperature profile, and the actual SO_2 height, a way to solve this would include an iterative process using a standard weighting function for the first inversion iteration as an estimate of the SO_2 heights. After the first iteration (which is done exactly as now), the estimated height profile (and if necessary other information, e.g., temperature and humidity) would be known for every grid cell. Subsequently, a radiative transfer model (or possibly simpler calculations) should be used to recalculate the weighting functions based on temperature and water vapour as well as the estimated SO_2 heights. Thus a weighting function for each gridcell is calculated. In addition, it would be possible to determine the uncertainties associated with the individual observations (grid cells) so for every satellite observation different uncertainties could be specified (and not one standard error for the total domain as used until now). This is important especially when using AIRS satellite data. Low-level plume observations should have a higher uncertainty than observations at an altitude where the satellite instruments are more sensitive. When a weighting function and uncertainty for each grid cell is determined after the first iteration, the next iteration will use these recalculated values and another inversion is performed, presumably with higher accuracy.

The height of absorber peak was also allowed to change for the analytic weighting function, ranging from about 8 to 12 km. However, changing the peak the weighting function only affects the lowest level emissions, mostly below 6 km. As the height of absorber peak increases, the sensitivity of the lowest layers are decreased which in turn blows up the low level emissions for the same reason as explained with the previous weighting functions.

4.8 SO_2 decay by OH reaction and dry deposition

To investigate how the SO_2 mass decay by OH reaction and dry deposition is handled by the model, three different model simulations were executed with and without removal processes. First, no removal processes were considered, secondly removal of SO_2 by reaction with OH was considered, as described in chapter 3.1.1. Finally, a model simulation with removal by both OH and dry deposition was carried out.

Subsequently, the e-folding lifetime for SO_2 for each simulation was calculated. The e-folding time refers to the time interval in which the initial SO_2 mass has decayed by a factor of e. (Only the SO_2 emissions from the volcano are considered, and no background SO_2 or anthropogenic emissions.) The results are shown in figure 4.19. The SO_2 mass with time, without considering removal processes, is constant at a value slightly below 1.2 Mt. When OH reaction is considered the SO_2 mass decreases exponentially with time, and the e-folding time is 24 days. Considering SO_2 decay both by OH reaction and dry deposition, the decay is even stronger, and the e-folding time is 22 days. It is clearly the OH reaction that contributes to the largest decrease of SO_2 mass.

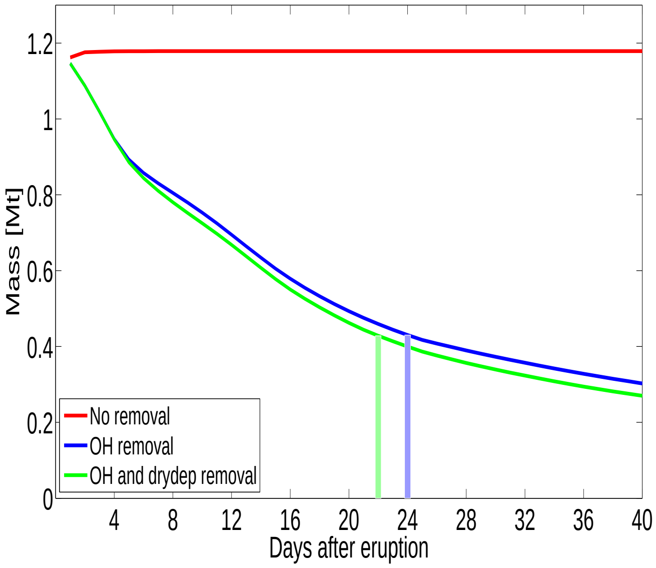

Figure 4.19: *Total mass of SO_2 [Mt] obtained from various FLEXPART simulations with and without removal processes considered. The light coloured lines locate the respective e-folding times for the different simulations.*

As pointed out in the methodology chapter, wet deposition was not considered as a loss due to the minor importance of this sink. SO_2 in the troposphere is also lost by aqueous oxidation by O_3, H_2O_2 and HO_2NO_2 and these loss reactions obviously also affect the lifetime of SO_2, but they were not considered in the model simulation.

Dry deposition presumably depends mostly on the height of the plume. As seen from the inversion profile in figure 4.1(b), there are only minor emissions below 3 km so it is first when the plume descends to the surface layer that dry deposition becomes significant. Calculation of the lifetime when considering loss of SO_2 only by dry deposition gives an e-folding time of 264 days, which implies that most of the SO_2 is at high altitude.

Calculations of the e-folding times for the troposphere and stratosphere separately gives approximately 15 days for the troposphere and 47 days for the stratosphere, when considering both reaction with OH and dry deposition, and a tropopause height at 10 km.

As mentioned in chapter 2.3, the lifetime of SO_2 in the troposphere is on the order of a few days, while in the stratosphere the lifetime is on a order of weeks. Bluth et al. (1997) made model calculations to estimate the potential aerosol loading to the stratosphere from explosive volcanic eruptions. For the average conversion rate of stratospheric SO_2 to sulphate aerosol they used an e-folding time of 35 days, which was in good agreement with other published values, all of which was within the range of 30-40 days. For the troposphere, Berglen et al. (2004) estimated the global lifetime of SO_2 to 1 day using the OsloCTM2 model, OH and dry deposition contributed to 8.8% and 46.2% of the loss, respectively, and the loss by dry deposition was high compared to other model calculations. Furthermore, Brasseur et al. (1999) used an OH concentration of 8×10^5 molecules cm^{-3} and a rate coefficient of 9×10^{-13} cm^3 molecule^{-1} s^{-1} for the OH reaction, to calculate the lifetime of SO_2 which results in approximately 16 days. The reaction rate used for this model simulation was, as mentioned in section 3.1.1, set to $1.35 \times 10^{-12} cm^{-3} s^{-1}$. Using the same OH concentration as Brasseur et al. (1999), the lifetime of SO_2 with this reaction rate is approximately 11 days.

The loss of SO_2 by reaction with OH depends obviously on the amount of OH present. OH is the most important oxidant in the daytime chemistry, and in the troposphere OH is initially formed by reactions with O_3 and sunlight, and further with H_2O. OH has maximum at low latitudes due to the the high abundance of water vapour and strong incoming solar radiation in this region. The Kasatochi Volcano is located at ~52° N which imply that there is not as much OH present than at the equatorial regions, and hence the lifetime of SO_2 emitted by Kasatochi will be longer.

Based on the comparison with other studies, the fact that the Kasatochi volcano are located quite far north, the low loss rate by dry deposition due to high altitude emissions, and also that not all SO_2 sinks are considered, the lifetimes calculated from the FLEXPART simulation, are in agreement with the suggested SO_2 lifetimes.

4.9 Errors and uncertainties

In the following a general discussion of the uncertainties and sources of errors arising from the various parts of the inversion method is given. Some of which are already mentioned in the previous chapters. However, the high importance of these uncertainties makes them worth repeating and to put them in context.

First, the satellite data used in the inversion method are concerned with uncertainties. In general, this involves the fact that there are restrictions on the satellite retrievals. For example for AIRS, the satellite retrievals are restricted to the UTLS, thus the measurements do not give any information on the lower tropospheric SO_2 (or mid/upper stratosphere).

The accuracy of the satellite measurements has to be specified and with lack of detailed information regarding the standard errors of the observations, only one standard error for each instrument is specified. The standard error for the AIRS observations is evaluated to 3 DU, which is the actual measurement error. However, this might be too low because this value would possibly better fit an atmosphere where there is little water vapour and cloud interference (as in the previous case study of the eruption of Jebel At Tair). The retrieval errors for AIRS are specified in the paper by Prata and Bernardo (2007). In summary the error sources include radiometric accuracy of the AIRS channel (1 DU), estimation of the background absorbance spectrum (4 DU), interference from clouds and other gases (principally water vapour) (4 DU), height errors (2 DU) and errors in the spectroscopic parameters (1 DU), giving a total of 6 DU. For OMI, which provides rather accurate measurements, the standard error is set to 2 DU, which includes the measurement uncertainties and some variable deviations in the OMI retrieval, as well as an assumption that for the comparison of model simulations with OMI the larger part of the misfit stems from the model simulation. The accuracies for the OMI retrieval are described by Yang et al. (2007). Ideally the standard errors should be specified for each receptor element (each grid point in the domain). For example for AIRS, the standard error should be high when SO_2 is located at low levels due to the restriction of the satellite retrievals. Also the standard errors should not only contain the measurement error but rather a standard misfit between the observations and the model results.

The uncertainties for the a priori values are specified for each source term. The uncertainties are generally taken as proportional to the respective emission value, but for some parts of the emission profile the uncertainties are changed and allow substantial corrections to the initial profile. If the a priori uncertainties are low, the a posteriori profile will follow the a priori profile closely. However, the same principle applies for the uncertainties of the observations, which together with the uncertainties in the a priori "weigh" the influence of the a priori against the measurement-model misfit. An important consideration is the ratio between the two uncertainties.

Another important issue concerns the independency of the satellite observations. The inversion method assumes that the measurements are uncorrelated, meaning that the value of one particular observation (pixel) is independent of the neighbouring pixels. In reality this is clearly not the case, and this can also lead to errors.

Furthermore, the weighting function applied to the FLEXPART data used in the inversion method is a source of uncertainties and errors. This is previously elaborated and imply that if the sensitivity to low altitude mass loadings is very low, this can blow up the emissions at this altitude. Similar to the standard errors of the observations, the weighting function should ideally be specified for each grid point (receptor element). As previously explained this can be implemented by an iterative process which uses the estimated SO_2 heights (and other information) to perform recalculations.

Additionally, the satellite data were approximated to the nearest hour for comparison with the corresponding model data. This is also an approximation that can affect the results. However, given that the maximum modification for the times was about 20 minutes it would probably not influence the results considerably.

The eruption time (or the time when the emissions were effectively injected into the atmosphere) is of unknown accuracy and can potentially lead to errors. Especially for the eruption of Kasatochi, which erupted several times during the first six hours, the assumed eruption onset and the assumption that all SO_2 is emitted at once, can cause unreal emissions. Given the following example, this inaccuracy can cause increased low level emissions. It is assumed that all mass is emitted at once at 22:30 UTC. Imagine that the actual mass of the second eruption at 01:50 UTC is visible in the satellite observations a few hours later. This mass will clearly not have been transported very far since it was released at 01:50 UTC. But assuming that this mass is released at 22:30 UTC, the model transports this mass over a greater distance than in reality. The satellite measures some SO_2 in the vicinity of the volcano, thus this SO_2 is not transported far. If there are some source-receptor elements that allow fitting the observations, the inversion method will say that the SO_2 observations probably originate from the lowest altitudes where transport is slowest. In reality the observations originate from the second eruption of the volcano and could have been emitted at an higher altitude where winds are stronger because in reality it is not transported for such a long time. This way, the uncertainty of the eruption time could lead to errors in the emission height profile. In the future, this can be accounted for by allow the inversion method to determine not only one vertical profile but several when considering different emission times. Moreover, the winds at low altitude are generally more slow, thus the transport is slow, and potentially many possibilities of emission heights can fit the observed pattern measured by the satellite, and the result can be high emissions at low altitudes.

Also, the errors in the model simulation with FLEXPART grow with time due to errors in the underlying wind fields, interpolation errors, self-heating of the plume, etc. Another consideration includes the vertical and horizontal resolution used for the model simulation in the inversion method. For this study a horizontal resolution of $1° \times 1°$ and a vertical resolution of 500 metres were used, while for the previous case study of Jebel At Tair a horizontal resolution of $0.3° \times 0.3°$ and 150 metres vertical resolution were used. The consequence of using a different resolution was not considered in this study. However, the optimal resolution should be a case for further study.

In the future, improvements regarding the uncertainties of the inversion method will be an important part of work. A better characterization of the uncertainties and particularly include a posteriori uncertainties is essential.

Chapter 5

Summary and conclusion

An inversion method was used in this study to estimate the vertical profile of SO_2 emissions from volcanic eruptions. Basically, this was done by using total column measurements of SO_2 from satellites and a Lagrangian dispersion model, FLEXPART. The method was applied for the eruption of Kasatochi Volcano in August 2008 which emitted an estimated 1.2 Mt of SO_2 to the atmosphere. The satellite instruments utilised in this case study were AIRS and OMI, which observed the volcanic plume up to two weeks after the eruption. A summary and important concluding remarks from this study are as follows:

- The first estimated height emission profile of SO_2 was obtained by using total column data from AIRS for 3 days after the eruption. Emission maxima were found at ∼5 km a.g.l, between ∼9 km and ∼15 km and at ∼18 km. According to this inversion, approximately 36% of the mass of SO_2 was injected above the tropopause located slightly below 10 km. The AIRS satellite data did not provide any constraints for the estimated emissions below 3 km and above 22 km, as suggested by the infrared weighting function. The emission peak around 5 km was very high and of uncertain accuracy due to the restrictions on the lower tropospheric SO_2 detection by AIRS.

- OMI data for roughly 2 days after the eruption were used for a second inversion which yielded emission maxima near ∼4 km, ∼6 km, ∼8 km and ∼12 km, and smaller emissions between 15 and 20 km. According to this inversion, approximately 54% of the mass of SO_2 was injected above the tropopause. Emissions above 22 km were not constrained by the satellite measurements. The high emission peak around 5 km in the AIRS inversion was strongly reduced when using OMI data, also this emission peak was divided into two peaks at 4 and 6 km. Due to the higher accuracy on low-level SO_2 for OMI, the lower emissions were likely to be more accurate than when using AIRS data.

- Both a vertically constant and a non constant a priori profile were used for the inversions. The inversion profile was quite robust against changes in the a priori profile, especially when using OMI data.

- The estimated emission height profiles showed good agreement with height emission profiles from independent studies, such as estimates based on a trajectory ensemble technique (Maerker et al., 2008), and also using correlation coefficient calculations for comparison of simulated and observed plumes (Theys et al., 2009).

- The dispersion of the SO_2 plume was simulated by FLEXPART using emissions according to the estimated AIRS inversion profile for the non constant a priori profile case. The plume spread mainly southeastward from the volcano and was transported into a circular shape due to a passing cyclone. The plume was further transported towards the coast of Alaska where it split into two and traversed the North American continent in two "tails" before reaching the Atlantic Ocean and then reached Europe within a week after the eruption.

- Comparing the transport simulation using the inversion profile, with simulation using a uniform emission profile with realistic plume top altitude for SO_2 showed rather similar spatial pattern, however the actual mass at each grid point and in each height level was different.

- The simulated plume, using the estimated height emission profile, was compared to independent AIRS and OMI observations, as well as GOME-2 measurements. There were overall good agreements between the simulated plume and the observation. However, quantitatively the simulated plume showed some discrepancies to the observations, generally underestimating some parts of the SO_2 plume.

- Using LIDAR measurements in a qualitative manner to evaluate the plume height, the FLEXPART simulation of the plume showed very good agreement with observations from Nova Scotia 14-15 days, and from Svalbard up to 27 days after the eruption. The height of the modelled plume agreed with the observations to within $\sim$1 km. The LIDAR measurements from Nova Scotia showed an observed layer at 18 km height, it was indicated that this layer originated from emissions around 18 km, thus the LIDAR measurement demonstrated that SO_2 was injected to an altitude of 18-20 km by the volcanic eruption.

- Sensitivity experiments were carried out regarding the amount of satellite observations needed to obtain a meaningful height emission profile. It seemed that satellite data from one or two days after the eruption rather than using data for three days, would have sufficed to give relatively good results for the height emission profile. Using only one satellite overpass gave a relatively good estimate for the profile above 10 km, but the emissions below this altitude were reduced.

- Sensitivity studies for the effect of the weighting function were also performed. This showed that the low level emissions were critically sensitive to the weighting function. As the sensitivity at low altitudes decreased, the emissions at this height range increased. In the future, this should be improved by applying an iterative process which recalculates the weighting functions, as well as the uncertainties of the observations, based on the estimated SO_2 heights.

- The SO_2 mass decay by OH reaction and dry deposition estimated by the model, was investigated by calculating the e-folding times of SO_2. Considering both sinks, the lifetime was calculated to 15 days for the troposphere and 47 days for the stratosphere, which were in agreement with other studies. Due to the high altitude of the SO_2 plume, dry deposition was nearly negligible.

The inversion method presented can provide information needed in order to calculate the actual and future position and extent of volcanic plumes. This information can be utilised in near real-time applications by e.g., the VAACs to rapidly issue warnings on volcanic ash hazards. As soon as satellite data are available for the eruption, the inversion method can be applied and the results can be ready within minutes to a few hours. The time-critical part is the requirement of satellite data for the times recently after the eruption. For this purpose, geostationary satellites can provide excellent information (since they orbit at the same angular velocity as the Earth, thus sees the same part of the Earth all the time). For example, the Spinning Enhanced Visible and Infrared Imager (SEVIRI) instrument on board the Meteosat Second Generation (MSG) geostationary satellite, is continuously imaging the whole of Europe and all of Africa, and has a baseline repeat cycle of 15 min and a spatial resolution of 3 km. This short time resolution makes it very encouraging for operational use with the inversion method. Other useful geostationary satellites includes Geostationary Operational Environmental Satellite (GOES) which covers the U.S, and Geostationary Meteorological Satellite (GMS) imaging Japan and the surrounding areas.

The method presented can also be utilised for less time-critical studies, such as facilitating the understanding of the climatic impacts of stratospheric SO_2 injections by volcanic eruptions. The last major eruption with significant climatic influence was the eruption of Mount Pinatubo in 1991 which emitted about 30 Mt of SO_2 to the atmosphere that reached an altitude of more than 30 km. With the estimates based on this study approximately 0.5 Mt of SO_2 was injected into the stratosphere to an altitude of $\sim$20 km by the eruption of Kasatochi. An interesting question is whether this eruption will give a noticeable climatic effect, an issue investigated by Kravitz et al. (2008). They used the NASA Goddard Institute for Space Studies ModelE general circulation model to calculate the expected climate response to the resulting sulphate aerosol cloud, and conclude that the resulting cooling and changes in the stratospheric circulation would be difficult to detect. The results were presented at the American Geophysical Union Fall Meeting in December 2008 but are yet to be published in a journal. Furthermore, the proposed geoengineering techniques, a way to compensate for increasing greenhouse gas concentrations, require extended research and understanding before possibly being realised. The inversion method can contribute in such part of research.

Further improvements of the inversion method include reimplementation with volcanic ash aerosol mass instead of SO_2. This would allow the VAACs to improve the operational warnings given to aircraft pilots about volcanic ash avoidance. For this study, the SO_2 was only used as a proxy for ash. It would also be interesting to investigate the suggested separation of SO_2 and ash. Furthermore, a tracer for the oxidation product of SO_2 - sulphate, potentially also a hazard for aircraft, could be implemented. In addition, other sinks for SO_2 (apart from reaction with OH and dry deposition) should be considered. Furthermore, an iterative scheme recalculating weighting functions and observation uncertainties is to be implemented. Additionally, when the time of the eruption onset is unknown, incorporation of a procedure considering several emission intervals, subsequently optimise the vertical and temporal emission distribution, should be considered.

Bibliography

Alaska Volcano Observatory (2008) *A*laska Volcano Observatory. Kasatochi Eruption Page. Accessed Aug-Dec, 2008. http://www.avo.alaska.edu/activity/Kasatochi.php.

Berglen, T.F.; Berntsen, T.K.; Isaksen, I.S.A. and Sundet, J.K. (2004) *A* global model of the coupled sulfur/oxidant chemistry in the troposphere: The sulfur cycle. Journal of Geophysical Research, Vol. 109(D19310). doi: 10.1029/2003JD003948.

Bernard, A. and Rose, W.I. (1984) *T*he injection of sulfuric acid aerosols in the stratosphere by the El Chichon volcano and its related hazards to the international air traffic. Natural Hazards, Vol. 3: p. 59–67. doi: 10.1007/BF00144974.

Bey, I.; Jacob, D.J.; Yantosca, R.M.; Logan, J.A.; Field, B.D. and et. al (2001) *G*lobal modeling of tropospheric chemistry with assimilated meteorology: Model description and evaluation. Journal of Geophysical Research, Vol. 106(D19): p. 23 073–23 095O. doi 10.1029/2001JD000807.

Bluth, G.J.S.; Rose, W.I.; Sprod, I.E. and Krueger, A.J. (1997) *S*tratospheric Loading of Sulfur from Explosive Volcanic Eruptions. The Journal of Geology, Vol. 105: p. 671–683.

Bluth, G.J.S.; Schnetzler, C.C.; Krueger, A.J. and Walter, L.S. (1993) *T*he contribution of explosive volcanism to global atmospheric sulphur dioxide concentrations. Nature, Vol. 366: p. 327–329.

Brasseur, G.P.; Orlando, J.J. and Tyndall, G.S. (1999) *A*tmospheric Chemistry and Global Change (Oxford University Press). p. 123-124, 196-201, 251-254, 349-372, 508-509, 530-533. ISBN: 0-19-510521-4.

Bursik, M. (2001) *E*ffect of Wind on the Rise Height of Volcanic Plumes. Geophysical Research Letters, Vol. 28(18): p. 3621–3624.

Carn, S.A.; Krotkov, N.A.; Yang, K.; Hoff, R.M.; Prata, A.J.; Krueger, A.J.; Loughlin, S.C. and Levelt, P.F. (2007) *E*xtended observations of volcanic

SO_2 and sulphate aerosol in the stratosphere. Atmospheric Chemistry and Physics Discussion, Vol. 7: p. 2857–2871.

Carn, S.A.; Krueger, A.J.; Krotkov, N.A.; Yang, K. and Evans, K. (2008a) *T*racking volcanic sulfur dioxide clouds for aviation hazard mitigation. Natural Hazards. doi:10.1007/s11069-008-9228-4.

Carn, S.A.; Prata, A.J. and Karlsdottir, S. (2008b) *C*ircumpolar transport of a volcanic cloud from Hekla (Iceland). Journal of Geophysical Research, Vol. 113(D14311). doi:10.1029/2008JD009878.

Chahine, M.T.; Pagano, T.S.; Aumann, H.H.; Atlas, R.; Barnet, C. and et. al (2006) *A*IRS: Improving Weather Forecasting and Providing New Data on Greenhouse Gases. Bulletin of the American Meteorological Society, Vol. 87(7): p. 911–926. doi:10.1175/BAMS-87-7-911.

Crutzen, P. (2006) *A*lbedo enhancement by stratospheric sulphur injections: A contribution to resolve a policy dilemma?. Climatic Change, Vol. 77: p. 211–220. doi: 10.1007/s10584-006-9101-y.

Eckhardt, S.; Prata, A. J.; Seibert, P.; Stebel, K. and Stohl, A. (2008a) *E*stimation of the vertical profile of sulfur dioxide injection into the atmosphere by a volcanic eruption using satellite column measurements and inverse transport modeling. Atmospheric Chemistry and Physics, Vol. 8: p. 3881–3897.

Eckhardt, S.; Stohl, A.; Frank, A.; Seibert, P. and Wotawa, G. (2008b) *U*ser guide: The Lagrangian particle dispersion model FLEXPART 8.0. Technical report, NILU.

ECMWF (2002) *E*dited by: White, P.W.: IFS Documentation, ECMWF. Reading, UK. Available from: http://www.ecmwf.int.

Emanuel, K.A. and Živković Rothman, M. (1999) *D*evelopment and evaluation of a convection scheme for use in climate models. Journal of atmospheric Sciences, Vol. 56: p. 1766–1782.

Forster, C.; Stohl, A. and Seibert, P. (2007a) *P*arameterization of convective transport in a Lagrangian particle dispersion model and its evaluation. Journal of applied meteorology and climatology, Vol. 46: p. 403–422. doi: 10.1175/JAM2470.1.

Forster, P.; Ramaswamy, V.; Artaxo, P.; Berntsen, T.; Betts, R.; Fahey, D.W.; Haywood, J.; Lean, J.; Lowe, D.C.; Myhre, G.; Nganga, J.; Prinn, R.; Raga, G.; Schulz, M. and Dorland, R. Van (2007b) *C*hanges in Atmospheric Constituents and in Radiative Forcing. In: Climate Change 2007: The Physical Science Basis. Contribution of Working Group I to the Fourth Assessment Report of the Intergovernmental Panel on Climate Change. [Solomon, S., D. Qin, M. Manning, Z. Chen, M. Marquis, K.B. Averyt, M.Tignor and H.L. Miller (eds.)]. Cambridge University Press, Cambridge, United Kingdom and New York, NY, USA.

Graf, H.-F.; Li, Q. and Giorgetta, M.A. (2007) *V*olcanic effects on climate: revisiting the mechanisms. Atmospheric Chemistry and Physics, Vol. 7(17): p. 4503–4511.

Halmer, M.M. and Schmincke, H.-U. (2003) *T*he impact of moderate-scale explosive eruptions on stratospheric gas injections. Bulletin of Volcanology, Vol. 65: p. 433–440. doi: 10.1007/s00445-002-0270-x.

Holasek, R.E.; Woods, A.W. and Self, S. (1996) *E*xperiments of gas-ash separation in volcanic umbrella clouds. Journal of Volcanology and Geothermal Research, Vol. 70: p. 169–181.

IPCC (2001) *C*limate Change 2001: The Scientific Basis. Contribution of Working Group I to the Third Assessment Report of the Intergovernmental Panel on Climate Change. [Houghton, J.T.,Y. Ding, D.J. Griggs, M. Noguer, P.J. van der Linden, X. Dai, K. Maskell, and C.A. Johnson (eds.)]. Cambridge University Press, Cambridge, United Kingdom and New York, NY, USA, 881pp.

Kravitz, B.; Robock, A.; Oman, L.; Stenchikov, G. and Marquardt, A. (2008) *C*limate Effects of the 2008 Okmok and Kasatochi Eruptions. American Geophysical Union Fall Meeting Abstracts, (A52A-03). Provided by the SAO/NASA Astrophysics Data System. Available from: http://adsabs.harvard.edu/abs/2008AGUFM.A52A..03K.

Krotkov, N.A.; Carn, S.A.; Krueger, A.J.; Bhartia, P.K. and Yang, K. (2006) *B*and Residual Difference Algorithm for Retrieval of SO2 From the AURA Ozone Monitoring Instrument (OMI). IEEE Transactions on Geoscience and Remote Sensing, Vol. 44(5): p. 1259–1266. doi: 10.1109/TGRS.2005.861932.

Liou, K.N. (2002) *A*n Introduction to Atmospheric Radiation, Vol. 84 (Academic Press, International Geophysics Series), 2 edition. ISBN: 0-12-451451-0.

Maerker, K.C.; Rix, P.V. M. and Geffen, J. van (2008) *T*rajectory matching and dispersion modeling of volcanic plumes utilizing space-based observations. In *I*EEE proceedings of the 2nd USEReST workshop, Naples, Italy, 2008.

Malo, A. (2008) *D*RAFT: Application of Atmospheric Long-Range Transport and Dispersion Modelling: Tracking Volcanic Ash Cloud and Sulfur Dioxide Gas Released from the August 2008 Eruption at Kasatochi Volcano, Alaska. Meteorological Service of Canada, Environmental Emergency Response Section.

Mankin, W.G.; Coffey, M.T. and Goldman, A. (1992) Airborne observations of SO_2, HCl, and O_3, in the stratospheric plume of the Pinatubo volcano in July 1991. Geophysical Research Letters, Vol. 19(2): p. 179–182.

McCormick, M.P.; Thomason, L.W. and Trepte, C.R. (1995) Atmospheric effects of the Mt Pinatubo eruption. Nature, Vol. 373: p. 399–404. doi: 10.1038/373399a0.

NASA (2008) NASA's Earth Observatory and Natural Hazards. Volcanoes, Aleutian Islands' Kasatochi Volcano Eruption Pages. Accessed Aug-Dec 2008. http://earthobservatory.nasa.gov/NaturalHazards/.

Oberhuber, J.M.; Herzog, M.; Graf, H.-F. and Schwanke, K. (1998) Volcanic plume simulation on large scales. Journal of Volcanology and Geothermal Research, Vol. 87: p. 29–53.

Olson, D.W.; Doescher, R.L. and Olson, M.S. (2003) When The Sky Ran Red: The Story Behind The Scream. Sky and Telescope magazine. Available from: http://www.skyandtelescope.com/about/pressreleases/.

O'Malley, J. and Bragg, B. (2008) Planes flying again after ash cancellations. Anchorage Daily News. Published August 11th, 2008. http://www.adn.com/news/alaska/story/490210.html.

OMI Sulfur Dioxide Group (2008) Daily OMI images. Accessed June-Dec 2008. http://so2.umbc.edu/omi/.

Prata, A.J. (2008) Satellite detection of hazardous volcanic clouds and the risk to global air traffic. Natural Hazards. doi: 10.1007/s11069-008-9273-z.

Prata, A.J. and Bernardo, C. (2007) Retrieval of volcanic SO_2 column abundance from Atmospheric Infrared Sounder data. Journal of Geophysical Research, Vol. 112(D20204). doi:10.1029/2006JD007955.

Prata, A.J.; Carn, S.A.; Stohl, A. and Kerkmann, J. (2007) Long range transport and fate of a stratospheric volcanic cloud from Soufrière Hills volcano, Montserrat. Atmospheric Chemistry and Physics, Vol. 7: p. 5093–5103.

Prata, A.J. and Kerkmann, J. (2007) Simultaneous retrievel of volcanic ash and SO_2 using MSG-SEVIRI measurements. Geophysical Research Letters, Vol. 34(L05813). doi: 10.1029/2006GL028691.

Rix, M.; Valks, P.; Hao, N.; Erbertseder, T. and Geffen, J. van (2008) *M*onitoring of volcanic SO_2 emissions using the GOME-2 satellite instrument. In *I*EEE proceedings of the 2nd USEReST workshop, Naples, Italy, 2008.

Robock, A. (2000) *V*olcanic eruptions and climate. In A. Robock and C. Oppenheimer (editors), *V*olcanism and the Earth's atmosphere, number 139 in Geophysical Monograph, p. 191–219 (American Geophysical Union, Washington, DC). ISBN: 0-87590-998-1.

Schneider, D.J.; Rose, W.I.; Coke, L.R. and Bluth, G.J.S. (1999) *E*arly evolution of a stratospheric volcanic eruption cloud as observed by TOMS and AVHRR. Journal of Geophysical Research, Vol. 104(D4): p. 4037–4050.

Seibert, P. (2000) *I*nverse modelling of sulfur emissions in Europe based on trajectories. In P. Kasibhatla; M. Heimann; P. Rayner; N. Mahowald; R.G. Prinn and D.E. Hartley (editors), *I*nverse Methods in; Global Biogeochemical Cycles, p. 147–154 (Geophysical Monograph 114, American Geophysical Union). ISBN: 0-87590-097-6.

Smithsonian Institution (2008) *G*lobal Volcanism Program. Accessed June-Dec 2008. http://www.volcano.si.edu/.

Stohl, A.; Forster, C.; Frank, A.; Seibert, P. and Wotawa, G. (2005) *T*echnical note: The Lagrangian particle dispersion model FLEXPART 6.2. Atmospheric Chemistry and Physics, Vol. 5: p. 2461–2474.

Stohl, A.; Hittenberger, M. and Wotawa, G. (1998) *V*alidation of the Lagrangian Particle Dispersion model FLEXPART against large-scale tracer experiment data, Vol. 32, p. 4245–4264 (Atmospheric Environment).

Stohl, A. and Thompson, D.J. (1999) *A* density correction for Lagrangian particle dispersion models. Boundary-Layer Meteorology, Vol. 90(1): p. 155–167. doi: 10.1023/A:1001741110696.

Textor, C.; Graf, H.-F.; Herzog, M. and Oberhuber, J.M. (2003) *I*njection of gases into the stratosphere by explosive volcanic eruptions. Journal of Geophysical Research, Vol. 108(D19): p. 4606. doi:10.1029/2002JD002987.

Theys, N.; Roozendael, M. Van; Dils, B.; Hendrick, F.; Hao, N. and Maziere, M. De (2009) *F*irst satellite detection of volcanic bromine monoxide emission after the Kasatochi eruption. Geophysical Research Letters, Vol. 36(L03809). doi:10.1029/2008GL036552.

VAAC (2008) *V*olcanic Ash Advisory Centers. http://www.metoffice.gov.uk/aviation/vaac/.

Volcano World (2008) *A*ctivity Cloud: Kasatochi. Accessed June-Dec 2008. http://volcanoworld.wordpress.com/tag/kasatochi/.

Wallace, J.M. and Hobbs, P.V. (2006) *A*tmospheric science; An Introductory Survey (Academic Press), 2 edition. ISBN: 13:978-0-12-732951-2.

Wang, X.; Boselli, A.; D'Avino, L.; Pisani, G.; Spinelli, N. and et. al (2008) *V*olcanic dust characterization by EARLINET during Etna's eruptions in 2001-2002. Atmospheric environment, Vol. 42: p. 893–905.

Weather Station History (2008) *H*istory for MADKA2, Adak Island, Alaska. Accessed January 2009. http://www.wunderground.com/weatherstation/.

Wesely, M.L. (1989) *P*arameterization of surface resistances to gaseous dry deposition in regional-scale numerical models. Atmospheric Environment, Vol. 23(6): p. 1293–1304. doi:10.1016/j.atmosenv.2007.10.058.

Wesely, M.L. and Hicks, B.B. (1977) *S*ome factors that affect the deposition rates of sulfur dioxide and similar gases on vegetation. Journal of Air Pollution Control Association, Vol. 27: p. 1110–1116.

Wigley, T.M.L. (2006) *A* combined mitigation/geoengineering approach to climate stabilization. Science, Vol. 314: p. 452–454. doi: 10.1126/science.1131728.

Yang, K.; Krotkov, N.A.; Krueger, A.J.; Carn, S.A. and Bhartia, P.K. (2007) *R*etrieval of large volcanic SO_2 columns from the Aura Ozone Monitoring Instrument: Comparison and limitations. Journal of Geophysical Research, Vol. 112(D24S43). doi: 10.1029/2007JD008825.